Journal of the Brazilian Society of Mechanical Sciences and Engineering (2022) 44:593
https://doi.org/10.1007/s40430-022-03889-x

TECHNICAL PAPER

Experimental and numerical investigation of conventional and stiffened re-entrant cell structures under compression

Mitat Öztürk[1] · Tarık Baran[1] · Mehmet Seha Tatlıer[2]

Received: 18 July 2022 / Accepted: 26 October 2022 / Published online: 23 November 2022

Abstract
A classical re-entrant cell is a type of metamaterial known as auxetic. While the most unusual and advantageous feature of auxetic materials is that they have negative Poisson's ratios, having low stiffness—as seen in the classical re-entrant cell—may be a drawback. A study was conducted to increase the stiffness of the classical re-entrant cell while maintaining the negative Poisson's ratio. This paper reports the nonlinear experimental and numerical works of three re-entrant cells one of which is a well-known classical re-entrant cell, and the latter two were modified based on classical re-entrant cell. In the work, the cellular structure specimens were fabricated with a 3D printer using polylactic acid (PLA) material and crushing tests were conducted until the full crush phase. The specimens were also modelled using solid finite elements considering wall-to-wall frictional contacts and analysed. The linear mechanical properties of the cells were also determined by employing analytical expressions that were developed for modified cells. Thus, both the theoretical and the nonlinear numerical results were validated using experiments. In conclusion, the modified cells exhibited an increase in stiffness, energy absorption capacity, and plasticity, compared to the classical re-entrant cell. All benefits and drawbacks of the modifications to achieve stiff cells are reported in this paper.

Keywords Re-entrant cellular structures · Auxetic · Energy absorption · Negative Poisson's ratio · Nonlinear crushing response

1 Introduction

Metamaterials are materials with the ability to tailor for the needs of the application. Due to the tuning ability, metamaterials have been investigated and improved for decades [1]. Cellular structures that a subgroup of metamaterials are advantageous in creating light-weight and high-strength structures because of their high stiffness/strength to mass ratios. Particularly honeycomb cellular structures have been used for decades as engineering materials in naval, bioengineering, aerospace, and automobile industries [1, 2]. Among all cellular structures, the most striking ones are auxetics. Auxetics are anisotropic materials that have a negative Poisson's ratio (NPR) owing to exhibiting transverse contraction under uniaxial compression and transverse expansion under uniaxial tension load [1]. In mechanics, Poisson's ratio is usually calculated as positive for linear elastic isotropic materials by definition; however, theoretically, Poisson's ratio values are given between − 1 and 0.5 in textbooks [3]. Poisson's ratio is calculated as negative for some natural and fabricated modern materials [4]. Ting and Chen state that the Poisson's ratio of anisotropic materials can be theoretically unlimited, and metamaterials can be designed for desired mechanical properties [5]. As well as they can be found in nature, auxetics are mostly designed and fabricated metamaterials [1, 6–9]. Although Evans [10] first use the term "auxetic" for material having NPR, just a couple of years earlier Lakes had published his pioneering work covering materials with NPR [11].

Auxetic metamaterials can have cellular structures. When it comes to cellular structure, NPR is closely related to the

Technical Editor: João Marciano Laredo dos Reis.

Disclaimer: The authors declare to accept the disclaimer.

✉ Tarık Baran
tarikbaran@osmaniye.edu.tr

[1] Department of Civil Engineering, Osmaniye Korkut Ata University, 80000 Osmaniye, Turkey

[2] Department of Mechanical Engineering, Osmaniye Korkut Ata University, 80000 Osmaniye, Turkey

deformation of the structure. Considering the deformation mechanism of the unit cell, auxetic metamaterials can be classified into three main topics: (1) re-entrant cellular structures; (2) chiral structures; (3) rotating unit structures [1]. Among all cellular structures, the most researched group are the re-entrant cells that are derived from regular honeycomb cell by deforming the outward corners inward. One of the first study that proves theoretically and experimentally cellular honeycomb structures may have NPR was presented by Gibson et al. [12]. Later, Gibson et al. [2] published the first re-entrant cell structure's image in their textbook. Masters and Evans developed a general theoretical model to determine elastic properties of regular and re-entrant honeycomb cells based on flexure, stretching, and hinging deformation modes [13]. In the following years, many new types of auxetic cells have been derived from the re-entrant cell. Double-arrow cells have almost the same deformation mechanism as re-entrant cells: the deformation is governed by the inclined cell wall [14, 15]. A star-shaped auxetic cell has been generated by deforming the straight walls of a re-entrant cell. Iterative deformation of the walls increases the number of corners. Grima et al. [16] simulated the star-shaped cell behaviour in the molecular levels. Auxetic behaviour can be acquired by removing the regular rhombic cell walls: Smith et al. [17] presented the missing-rib auxetic structure obtained by removing the cell walls. Because they have tuning ability, mechanical properties of the auxetics can be set at desired values or material behaviour can be adapted for desired purposes, i.e. Poisson's ratios, elasticity modulus, shear modulus, and bulk modulus can be designed. Thanks to these properties, researchers have revealed unconventional properties, e.g. under the impact, auxetic material densifies at the impact zone in contrast to nonauxetics because of indentation resistance relation with the modulus of elasticity [18–21]. Lakes and Elms [22] have unveiled higher yield strength and energy absorption of auxetic foams than those of nonauxetic at the same density. Moreover, auxetic foams have a lower stiffness than nonauxetic ones. As reported by Dirrenberger et al. [23], the indentation resistance of auxetic cellular structures can be as high as regular honeycomb structures. Due to having synclastic curvature and high impact resistance, auxetics may be a useful lining material for spherical surfaces [24]. NPR bestows the auxetic materials a high shear strength and low bulk modulus. Theoretically, while Poisson's ratio is at the value of -1, the shear modulus will be infinite. Because of the potentially having an extraordinarily high shear resistance, many researchers have widely investigated the shear properties of the auxetics [25–30]. As stated by Choi and Lakes [31], although they have a smaller modulus of elasticity than nonauxetics, auxetics have a larger fracture toughness. Auxetic materials may have many uncovered possible employing fields. However, many research papers have unveiled application fields such as acoustic absorption, wave transmission, and vibration damping [32]. Due to the anisotropy, auxetics can be utilized for absorption, guidance, and transmission of acoustic waves [33–36]. Zhu et al. [37] reported that chiral auxetics effectively attenuates the vibrations. Investigations and potential designs of auxetics have been carried on the wave propagation by Bacigalupo and Gambarotta [38], Liebold-Ribeiro and Körner [39], Bacigalupo and De Bellis [40].

To obtain the cellular structures' material properties, a unit cell is theoretically modelled by the researchers [13, 41, 42]. Korner and Liebold-Ribeiro [43] have generated a systematic approach to identify whether the cell is auxetic or not by employing modal analysis. To obtain desired mechanical properties, mostly the cell topology has been modified. Besides, because the cellular structures are tiled in a pattern, different tile patterns have also been conducted to obtain desired mechanical properties. Most of the researchers have employed the experiments to verify their models generated using finite elements (FE), and they have often employed frame elements to model cell walls [44–57]. As an alternative to frame elements, shell and solid finite elements have also been utilized to obtain the linear and the nonlinear behaviour of cell walls [42, 58]. Some researchers have carried on their studies beyond the linear boundaries to acquire the cellular structures' energy absorption, damping capacity, etc. [22, 52, 59–62]. Determining the mechanical properties using the tiled cellular structure analysis leads to complexity on boundary conditions. Dirrenberger et al. [23, 47] have solved this complexity by employing periodic boundary conditions (PBCs). While determining the mechanical properties of core cell in periodically tiled cellular structure, the cell at the middle of the structure can be utilized with PBCs at the structure boundaries [23, 47, 63–66]. Some researchers have approached the complexity of cellular structures analysis using representative volume elements [67, 68].

Many of the most recent studies on auxetics have focussed on tuning the mechanical properties while preserving auxetic behaviour. Because of its simple and effective form, the re-entrant cell has been frequently preferred structure in deriving new cell types or modification works. Huang et al. [42, 69] have connected the different cell types using different connections to obtain zero and negative Poisson's ratios. Fu et al. [70] have obtained stiffness improvement by utilizing periodic auxetic structures in the unit cell walls. Li et al. [71] have reported a stiffness increment employing sine formed cell walls, and they related the period of walls and cell stiffness. Chen and Fu [72] achieved to tune the cell stiffness by connecting the cells with beams that have lower stiffness than cell walls. In a different work, Chen and Fu [73] have reported stiffness increment using a different approximation from their previous work: they have designed three new cells based on a re-entrant cell by combining both the middle of the straight walls and the inward corners. In their study, the

cell corners have been connected using first, a low-stiffness beam, second a small rhombus cell, and finally, these two structures together. Zied et al. [58] have achieved the stiffness increment by converting the straight cell walls to curved and elliptic forms. In their numeric and experimental work, Ingrole et al. [74] have studied the NPR and stiffness variation of the structures by building the structures with different cell types. To improve the tuning ability of the cell, Huang et al. [42] have connected the cells with thin plates that integrated into the straight cell walls. Their unusual tile pattern has endowed a wide range of parametric variation for tuning the cell material properties. Bezazi et al. [75] have acquired the stiffness increment by rounding the cell's sharp corners. Rayneau-Kirkhope [76] has reported an increased buckling strength and stiffness using lattice structures in the cell walls. Baran and Ozturk [77] have strengthened the cell by employing new parallel walls that support the existing inclined wall. With the new walls, the tuning parameters of the cell have been expanded. Tatlier et al. [78] have obtained the tuneable stiff cell by placing a circular beam that connects inward corners of the re-entrant cell. They have gained stiffer cell than conventional re-entrant cell while preserving the auxetic behaviour.

Because the tuneable metamaterials with auxetic behaviour can be employed in a wide range of areas, there are numerous works on auxetic materials and most of them focussed on improving cell stiffness and tuning ability. An example is taken from the textbook of Ratner et al. [79]: in the case of dentistry, if the tooth and filling material have the same stiffness while filling material has zero Poisson's ratio, a good interface will build between these two materials. Hence, the numerical and theoretical improvement works of new cells should be verified. And in practice, the advantages and disadvantages of the new cells should be revealed with limits of availability and tunability.

This paper reports an experimental verification and expanded numerical study of modified cells that were previously introduced by Baran and Ozturk [77] and Tatlier et al. [78]. In the following sections, modified cells have been reminded, and numerical models of the tiled structures have been introduced and validated. The experimental and numerical results of linear and nonlinear crushing behaviour of the structures have been reported. In the conclusion, superiorities and drawbacks of the new cells to the conventional re-entrant cell have been discussed.

2 Materials and methods

2.1 Test specimens and cell configurations

In this paper, the conventional re-entrant cell and modified cells will be entitled CRC, Type-I, and Type-II, respectively, as seen in Fig. 1. Figure 1 depicts the 3D printed tiled honeycomb structures samples using PLA filament in the first row. In the second row of Fig. 1, the CAD drawings with model dimensions and in the third-row core cells and definition parameters can be seen. The definition and numerical values of the cell parameters are noticed in Fig. 1g, h, i and are provided in Table 1. The red dots in Fig. 1 define the measurement points employed in the image processing. The loading direction is from the upside to the bottom side of the structures and the bottom side is fixed. All specimens include a PLA plate with 4.2 mm thickness that printed monolithically with the cells at the upper and bottom sides. All cells are designed as fixed to the PLA plates at the upper and bottom sides with a tile pattern of nine cells along the lateral direction and of five cells along the vertical direction. The right and left side of the specimens are free.

Because it is possible to verify the results of crushing modes of re-entrant structure experiments with the literature, we tested the classical re-entrant cell with different properties. The crushing modes of the classical re-entrant structure seen in Fig. 2b, d, and f are observed by Ingrole et al. [74]. After observing quite similar crushing modes with Ingrole et al. [74], the samples were printed with up and bottom PLA plates. Then, the test machine misalignment that leads to the failure seen in Fig. 2a was fixed. In the detail of Fig. 2, Fig. 2a, b, d, and f depicts post-experiment classical re-entrant structures. To investigate the scale effects, a scaled-down sample by a coefficient of 0.5 as seen in Fig. 2f was also tested. In the linear zone, the results of this sample derive the same results as for the full-scale structure when they are multiplied by 2. Figure 2c and e depicts the post-experiment crushing modes of Type-I and Type-II samples, respectively.

It is obvious that with annexed new walls, densities of the modified unit cells will increase. Hence, to indicate the density increment, the ratio of the density of modified cell (ρ) to the density of the CRC (ρ^*) is calculated as 2.8 and 1.78 for Type-I and Type-II, respectively.

Mechanical properties of the cell walls' base material PLA have been determined in accordance with the given calculation method in ASTM-D638-14 [80]. To identify the material properties of 3D-printed PLA walls, three dog-bone-shaped specimens were printed considering both the layers of walls and the layers of specimens being along the same direction. Dog-bone specimens were printed with at least four perimeter walls along the length. In addition, the infill density has a 100% fill rate and an angle of 45 degrees with the width of the samples. Figure 3a, b, and c depicts the employed dog-bone-shaped sample dimensions, 3D printed samples, and tensile testing, respectively. The stress–strain curves of the 3D printed PLA that can be seen in Fig. 4a were acquired from the tensile tests of the specimens and determined mechanical properties of the material can be

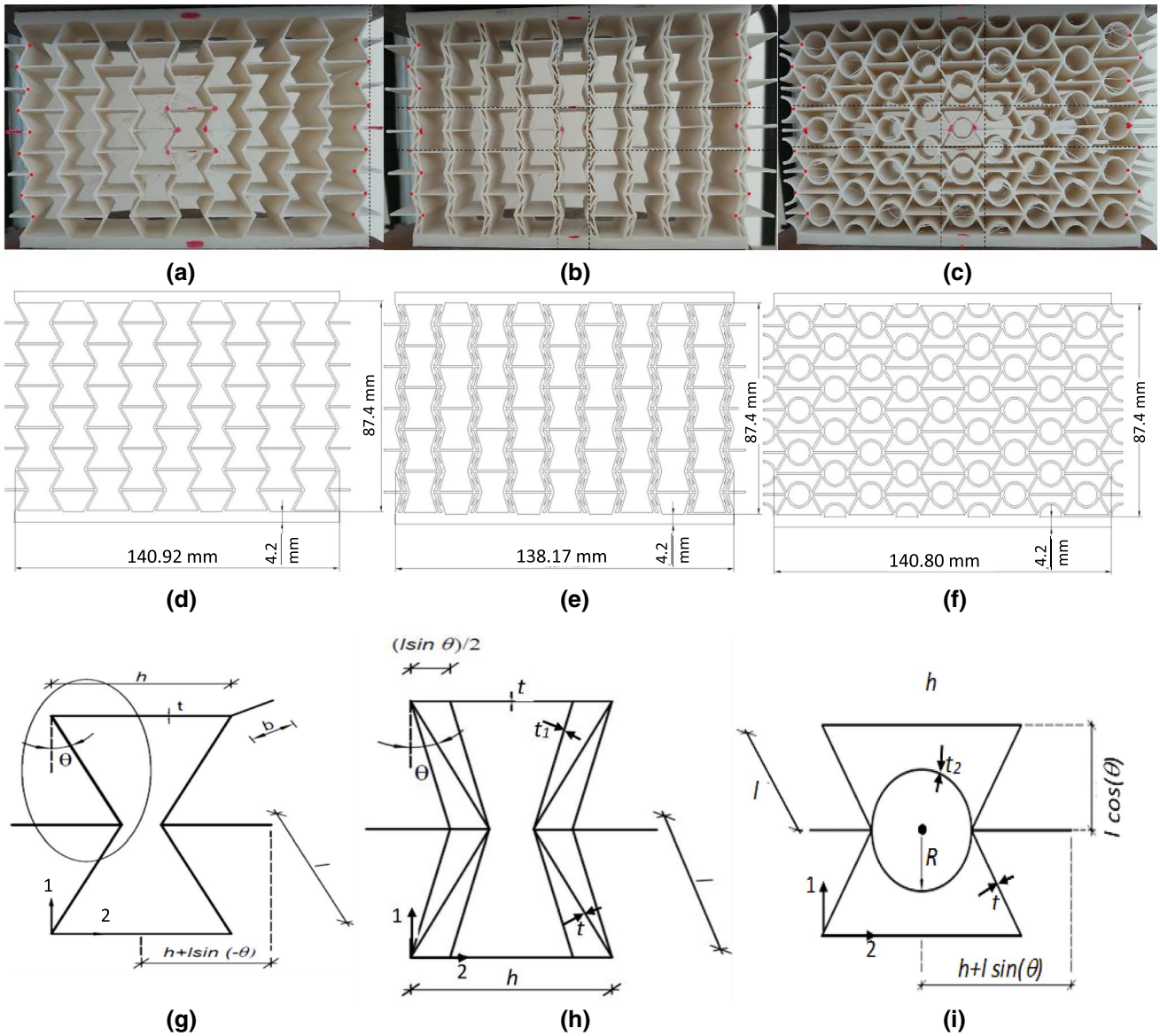

Fig. 1 3D printed re-entrant and modified honeycomb specimens, tiled structure dimensions, and unit cells: **a**, **d**, **g** conventional re-entrant cell; **b**, **e**, **h**, Type-I cell; **c**, **f**, **i**, Type-II cell

Table 1 Definition and values of unit cell parameters

Symbol	Definition	Value (wall axis-to-wall axis for lengths)
l	Cell inclined wall length (mm)	10
h	Cell height (mm)	20
θ	Cell angle (degrees)	−30
t	Cell wall thickness (mm)	0.8
t_1	New inclined wall thickness (only for Type-I) (mm)	0.8
t_2	New circular wall thickness (only for Type-II) (mm)	0.8
b	Cell width (mm)	40
$(l \cdot \sin\theta)/2$	Rigid zone length of Type-I cell (mm)	2.5
R	Circular wall radius of Type-II cell (mm)	5

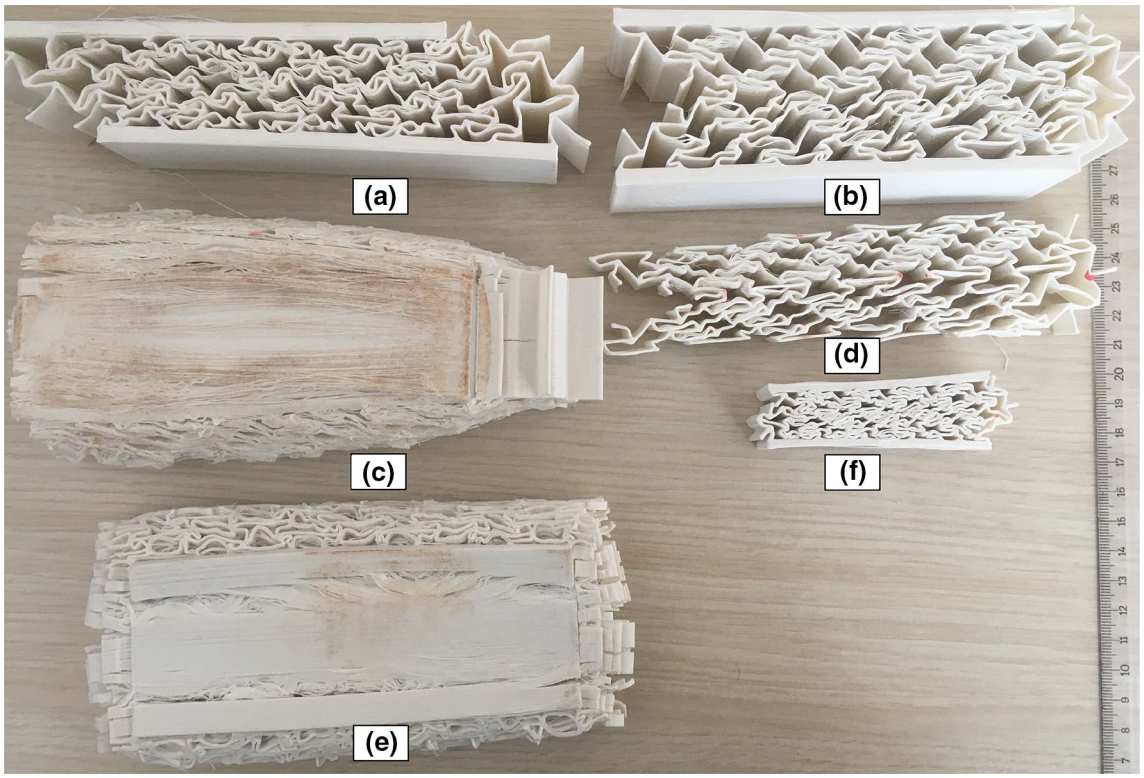

Fig. 2 Tested specimens in the experimental work

tracked from Table 2. The values in the last row of Table 2 are the mean values of mechanical properties obtained from samples. Determined properties were employed to model material nonlinearities in the numerical work. A bilinear softening material model [81] was employed in the numerical work to model strain softening which can be clearly seen in Fig. 4a. The strain-softening behaviour obtained in the experiments is quite similar to concrete behaviour [81]. Hence the strain-softening behaviour defined in the FE software was an adopted concrete model with the following parameters: open shear transfer coefficient is 0.30, closed shear transfer coefficient is 1.00, uniaxial cracking stress 16.01 MPa, uniaxial crushing stress is 31.33 MPa and tensile crack factor 0.6. The actual stress–strain relationship in Fig. 4a was used to determine for parameters. The material employed in FE analyses model stress–strain was obtained as depicted in Fig. 4b. There is also a sudden movement seen in the stress–strain plot that stems from the rapture of the dog-bone samples' perimeter walls at the lower strain range of [0.6–1%]. A quite similar 3D printed PLA material stress–strain relationship has been presented by Eutionnat-Diffo et al. [82].

In this work, all samples have been fabricated with a 3D printer with platform size of $300 \times 300 \times 300$ mm and nozzle diameter of 0.4 mm. The accuracy of the printer is ± 0.08 mm and PLA filament is defined as semi-flex.

2.2 FE models

The same CAD files used in the 3D printing process were also employed in numerical FE analysis. It is obvious that the large deflections and the contacts of the adjacent cell walls to each other will emerge with the increasing displacements. Solid elements were exerted to model cell walls in the nonlinear FE analysis because of having contact ability. A solid element is defined by eight nodes, and there are three translational degrees of freedom (DoF) at each node. The software's default contact algorithm is the pure penalty contact algorithm and can model surface-to-surface frictional contacts. This algorithm increases the total virtual work when the contact condition violation appears [83]. The wall-to-wall contacts were generated with a value of 0.4 friction. In the models, the displacements were applied to the structure at the top side of the network and the bottom side of the model has been assumed as fixed support. In all remaining parts of the model, translations along both 1 and 2 axes and rotations around the perpendicular axis (3 axis) were assumed as free and the other displacements were fixed to fulfil the in-plane behaviour. The material nonlinearity of PLA used to generate cell walls was modelled as bilinear softening material in compliance with values in Table 2 and Fig. 4. Geometric nonlinearity effects were enabled to model large deflections in all nonlinear FE analyses. Besides, the

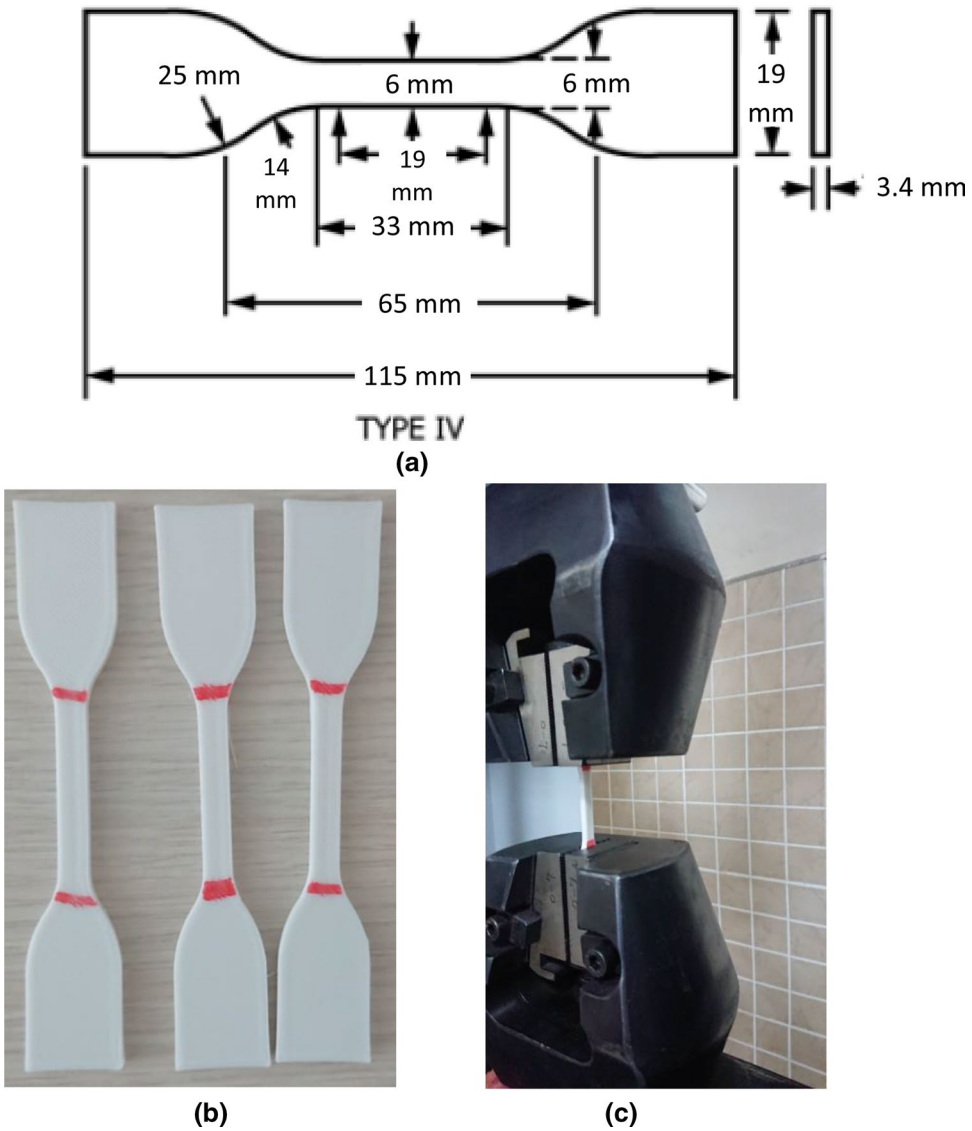

Fig. 3 **a** Dog-bone-shaped specimen dimensions (modified from ASTM-D638-14 [80]); **b** 3D printed dog-bone-shaped specimens; **c** dog-bone-shaped specimen tensile testing

following procedures were applied in the FE solver: Newton–Rapson algorithm was used with "Unsymmetric" key. Both the displacement and the rotation convergence options were activated with a convergence tolerance value of 0.5%. "Constant energy dissipation ratio" key with the programme default value of 1.0×10^{-4} was activated to ensure stabilization while using "Line Search" option in nonlinear analyses. While the bottom side was fixed, the displacement loading was applied from the top side of the model which was consistent with the loading rate used in the experiment.

2.2.1 Mesh optimization

Due to the obtained results from each solid element solution different from each other, a mesh optimization work was conducted. Figure 5 indicates a selected sample mesh pattern of the unit cell mesh for all types, and for Type-II cell tiled structure that the meshing process was the most challenging one. In the figure, *L* is the inclined cell wall's edge lengths and identical for all cell types, *H* is the cell height's edge lengths and identical for the CRC and Type-II. *H1* and *H2* are Type-I cell height's edge length parameters. *H* is defined for Type-I as $H = H1 + 2 \bullet H2$. Type-II cell parameter *RO* is the outer edge length of the circular wall that formed as a circular arc. *RI* is the full circular inner wall edge length. In Fig. 5, structure edges have also been defined with symbols, where *LS* is the structure's top and bottom plate's edge lengths. While meshing, they were divided into nine times larger than the number of *H* divisions. *W* is the edge length of both the structure and cell width that its actual value is 40 mm. It was divided into 2, 4, 8, and 16 in mesh optimization analyses. *T* is the top and bottom plate thickness with an actual value of 4.2 mm. Because of its expected rigid behaviour, it was not divided into multiple parts. In

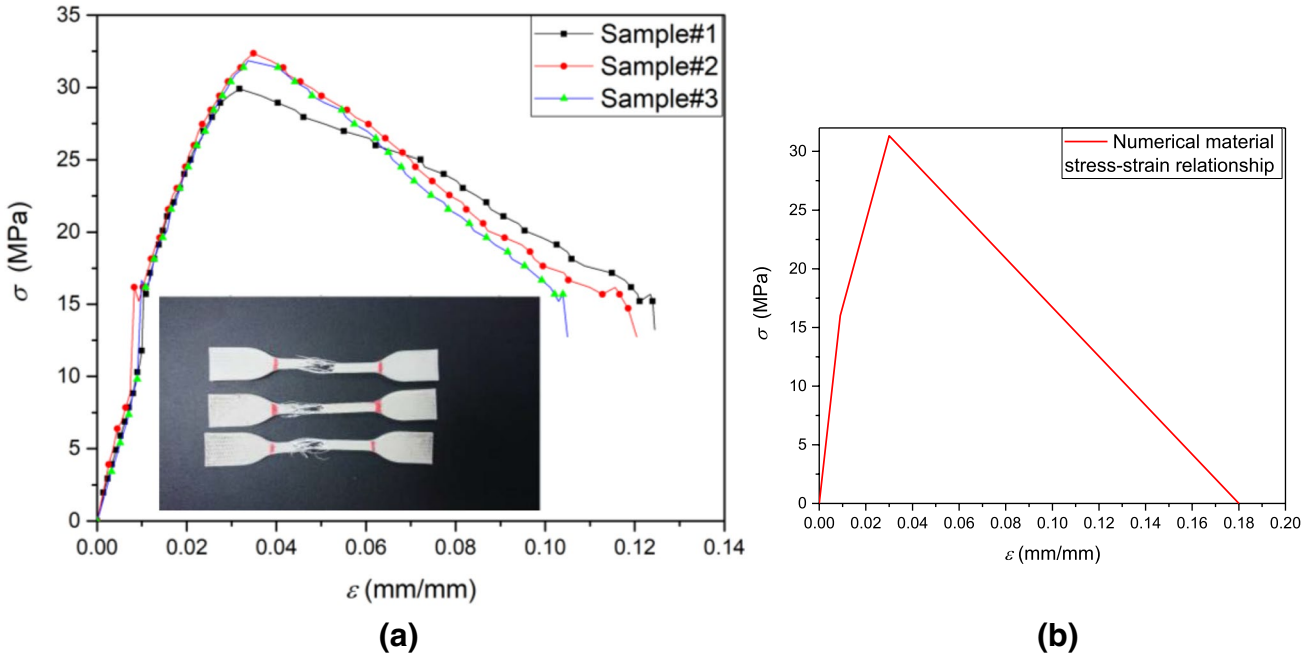

Fig. 4 **a** Stress–strain curves of dog-bone-shaped specimens, and **b** idealized stress–strain relationship for numerical analyses

Table 2 Mechanical properties of PLA material

	Density (kg/m^3)	Elasticity modulus (MPa)	Poisson's ratio	Bulk modulus (MPa)	Shear modulus (MPa)	Yield strength (MPa)	Tangent modulus (MPa)
Sample#1	1240	1132	0.34	1112.7	426.09	15.908	639.18
Sample#2	1240	1141	0.31	1115.2	428.95	16.075	642.65
Sample#3	1240	1135	0.35	1113.3	426.16	16.061	640.32
Mean	1240	1136	0.33	1113.7	427.07	16.01	640.72

the mesh optimization work, element edge lengths were generated using the inclined cell walls because they govern the deformation mode. The aim of the mesh optimization work is to generate well-shaped quadrilateral solid element faces at each segment of the cell by dividing wall lengths on 1–2 plane. All solid element edge lengths were remained very close to each other by using a proportional relationship with the cell wall lengths. Thus, only two parameters were tracked: the edge lengths of wall solid elements on 1–2 plane and the lengths of the solid element along the width. Because employing solid elements restricts the lengths of wall edges, the wall lengths vary from each other for different types of cells. Therefore, the lengths of inclined walls are 9.58 mm, 6.02, and 8.1 mm for CRC, Type-I, and Type-II, respectively.

In every analysis, the central cell strain along 2-axis was tracked. Total applied displacements along 1-axis were − 9.98 mm, − 9.87 mm, and − 10 mm for CRC, Type-I, and Type-II, respectively. Figure 6 depicts the mesh consistency analysis results. Each curve in the charts indicates how many parts edge length is divided into along the width. The element edge lengths were picked from the solution in which the central cell strain along 2 direction was steady. From Fig. 6, the consistent length of element edge was picked as 1.91 mm, 2 mm, and 1.62 mm for CRC, Type-I, and Type-II, respectively. The results of the mesh consistency analyses indicate that the solid element edge length does not depend on the number of elements along the width. At least four elements were employed in the width direction in all three models. The acquired edge lengths mean that the inclined wall edges divided into 5, 3, and 5 parts for the CRC, Type-I, and Type-II, respectively. With the given edge division numbers, the total element numbers employed in FE analyses are 2294, 5448, and 3998 for the CRC, Type-I, and Type-II, respectively. Besides this, the total node numbers are 18,345, 42,780,

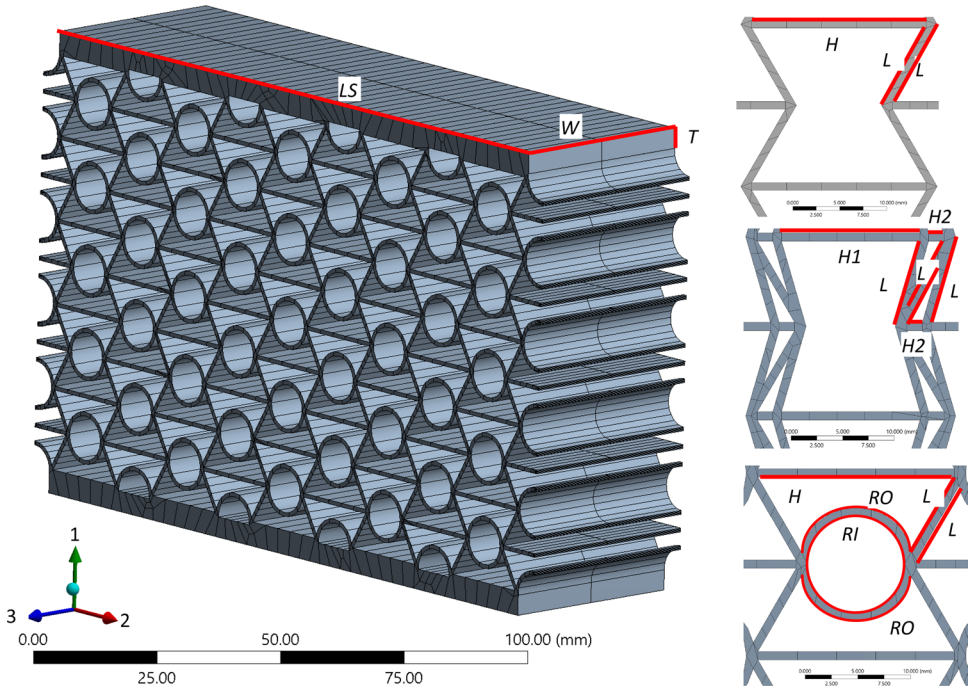

Fig. 5 Mesh view of tiled structure model (sample view taken from Type-II) and closer view of mesh for each type

and 31,995 for the CRC, Type-I, and Type-II analyses, respectively. Note that, a single element was employed across the thickness in the FE models. The FE models of this work employ a geometry file that models the problem domain as a single body to generate the mesh. This single body does not include a visible edge to control the mesh across the thickness. Due to the lack of the control edge, FE software did not achieve to divide the thickness into more layers. To eliminate the errors that lead from utilizing the one element across the thickness, the "full integration element control" option was activated in accordance with the FE software help documentation [83].

2.3 Experimental crushing test set-up

A universal test machine was used to perform the compression tests. The specimens were placed between a fixed flat steel plate and a compression plate. The loading increment was set up at 0.01 kN/s which corresponds to the value of displacement value of 20 mm/min. The loading was recorded by the universal machine itself. All specimens were loaded until the full crush phase. A high-resolution camera was also employed to monitor the displacement points of the specimens which are shown in Fig. 1a, b, and c with red dots. After taking the frames from the footage, all images were digitalized and flattened by the image processing. Thence, the values of the displacements were calculated to employ the evaluation of NPRs and stress–strain curves.

3 Results and discussion

3.1 Comparison of numerical and experimental results

3.1.1 Poisson's Ratios of Re-entrant cells

Poisson's ratios of the CRC, Type-I, and Type-II cells were calculated by employing previously given equations in the works of Baran and Ozturk [77], Tatlier et al. [78] and were compared to both the numerical and experimental results of this work. The Poisson's ratios of the numerical and the experimental analyses of this work were calculated from the footage at very early stages of the loading, i.e. structural behaviour was linear. Thus, the same linear condition was ensured for the calculation of Poisson's ratios as in the theoretical analyses. Two different video frames were extracted to calculate Poisson's ratios from experimental footage, and in the calculations, the mean values of tracking points (see Fig. 1a, b and c) were utilized both in the numerical and the experimental analyses as:

$$\varepsilon_{11} = (x_n - x_o)/x_o \tag{1}$$

$$\varepsilon_{21} = (y_n - y_o)/y_o \tag{2}$$

$$\nu_{12} = -\varepsilon_{21}/\varepsilon_{11} \tag{3}$$

where ε_{11} is the strain along 1 direction, x_n is the mean displacement of tracking points along 1 direction, x_o is the

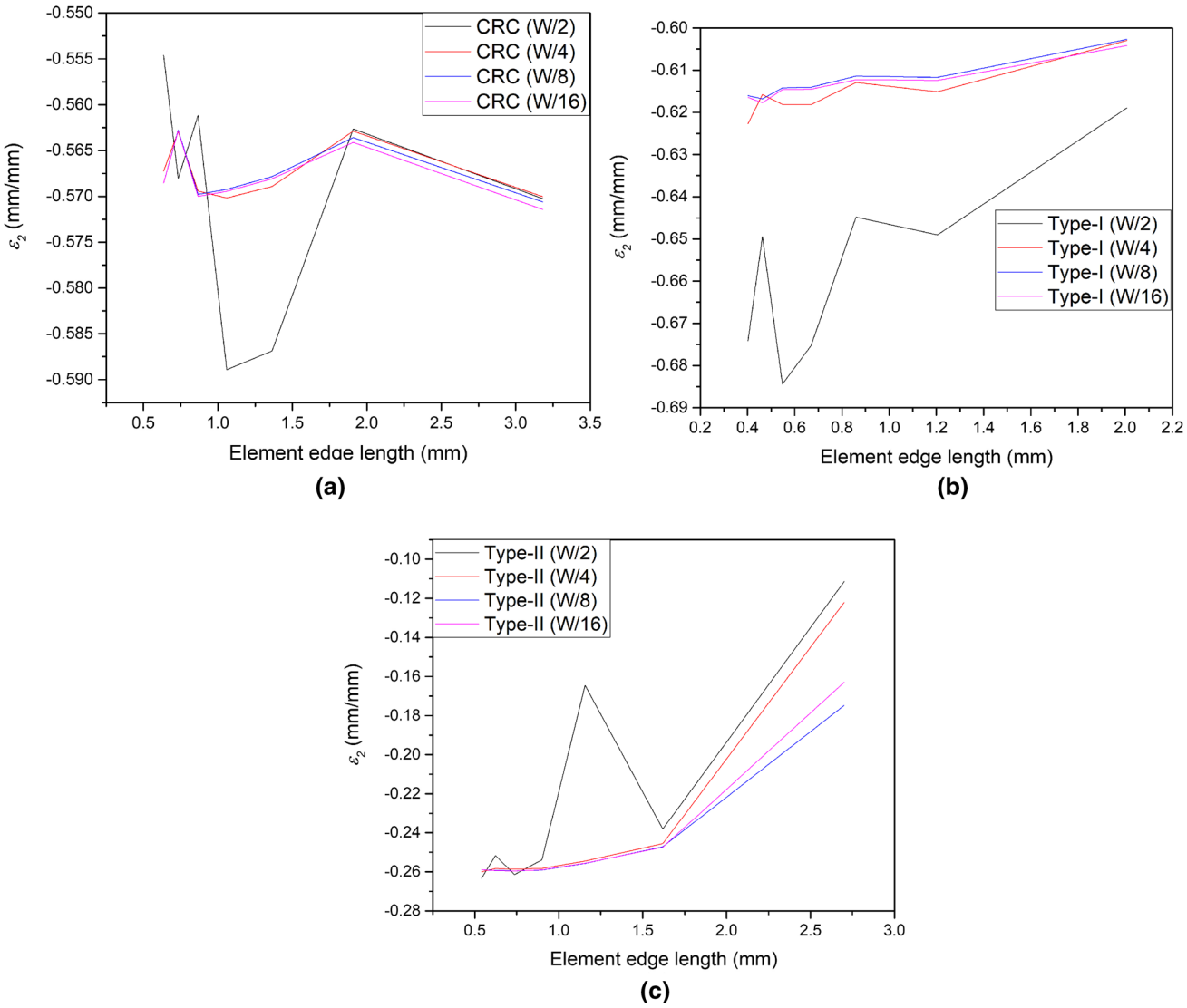

Fig. 6 Mesh optimization of results: **a** CRC tiled structure; **b** Type-I cell tiled structure; **c** Type-II cell tiled structure

undeformed length of structure along 1 direction, ε_{21} is the strain along 2 direction, y_n is the mean displacement of tracking points along 2 direction, y_o is the undeformed length of structure along 2 direction, and ν_{12} is the Poisson's ratio caused from loading along 1 direction.

From Table 3, quite closer results can be observed between the experiments and the numerical results when compared with theoretical results in column #6. This is an expected result since the solid element simulates the structure behaviour realistically. In the works of Baran and Ozturk [77], Tatlıer et al. [78], the cell walls are considered as a frame element and element lengths are substituted in the equations as axis-to-axis lengths. Even though this is not an inaccurate consideration, due to the rigid wall junctions, wall lengths should be downgraded to model the real values of lengths (see Fig. 1). If the inclined wall lengths and cell heights are substituted in the equations as axis-to-axis length, the results will be calculated as in Table 3 column #6. Roughly, the clear span lengths of inclined walls and cell heights can be calculated by subtracting half of the thickness from both ends of the wall. Nonetheless, complex junctions of modified cells force the measurement of the lengths from the CAD file. The measured inclined wall lengths were 9.076 mm, 6.03 mm, and 7.56 mm for the CRC, Type-I cell, and Type-II cell, respectively. In addition to shortened inclined wall lengths, the cell heights that also shortened were measured as 18.61 mm, 16.58 mm, and 18.61 mm for the CRC, Type-I cell, and Type-II cell, respectively. By substituting these values in the equations, closer results with the experiments were obtained as tracked from column #7. This finding is also coherent with the well-known effects of the thickness-inclined wall-length ratio on cell behaviour

Table 3 Calculated Poisson's ratios of re-entrant cells

ν_{12}	Experimental			Numerical	Theoretical with eqs. of Baran and Ozturk [77], Tatlier et al. [78]		Variation (%)			
	Frame#1	Frame#2	Mean		with axis-to-axis l and h	with clear l and h	$e = Abs\left(\frac{C\#4-C\#5}{C\#4}\right)\times 100$	$e = Abs\left(\frac{C\#4-C\#6}{C\#4}\right)\times 100$	$e = Abs\left(\frac{C\#4-C\#7}{C\#4}\right)\times 100$	
CRC	−0.987	−0.869	−0.928	−1.096	−1.021	−0.987	18.103	10.022	6.358	
Type-I	−1.013	−0.913	−0.963	−0.924	−1.393	−0.879	4.050	44.652	8.723	
Type-II	−0.644	−0.795	−0.720	−0.682	−0.922	−0.720	5.278	28.056	0	

that was stated by most of the researchers such as [13]. In Table 3, a small variation can be observed between column #6 and column #7 for the CRC theoretical results, because the clear wall length is quite close to the axis-to-axis length for the inclined wall. The given error rates in Table 3 prove that the experiments validate the theoretical equations which were previously presented by Baran and Ozturk [77] and Tatlier et al. [78], in linear region. It should be noted that because of the rigid wall junctions, substituting the clear lengths of cell walls in the theoretical equations provides a good match with experiments. The experiments also validate the numerical models of this work. Please refer the appendices for the equations of analytical model.

3.1.2 Crushing performance of conventional re-entrant, Type-I, and Type-II cells

Figures 7, 8, and 9 show in the first columns the randomly selected and extracted snapshots from experimental footage and equivalent histories with Von-Misses stresses from the numerical solution in the second columns. At first glimpse, a quite close behaviour is seen between experiments and numerical results except for Type-II: in the experiments and numerical analyses, both the CRC and Type-I crushed with an entire structure buckling. However, the Type-II crushed symmetrically without buckling in the experiment, while a buckling appears in the numerical analysis that was consistent with the numerical results of other types From Figs. 7, 8, 9, and 10, it can be interpreted that the materials of all three specimens yield quickly at the first stages of the loading; therefore, nonlinear behaviour also rises. Thus, all three specimens begin to crush as soon as crushing stress exceeded. Particularly, both Type-I and Type-II begin to crush earlier than the CRC because they are denser than the CRC and have more contact faces. The CRC tiled structure did not completely crush as seen from Fig. 11. Even, its induced deformation withdrew with a small amount as soon as unloading was starting. The other two types were able to load until their walls got into each other; however, the CRC loading was not succeeded to merge walls and the test machine stopped loading automatically.

From the detailed review of Figs. 7, 8, and 9, a one-way buckling behaviour can be observed. This finding is not surprising since the other researchers who worked with tiled cellular structures with or without rigid plates at the ends have reported similar results [74, 84–87]. Besides, the ruptures are observed at the rigid connection of the wall junctions. A similar result was previously reported in the work of Qi et al. [88]. Although the numerical models simulate the structural behaviour successfully, because of the laminated structure of walls, it was not possible to model wall ruptures that are particularly seen in Type-I (see Fig. 8, indicated with red ellipses).

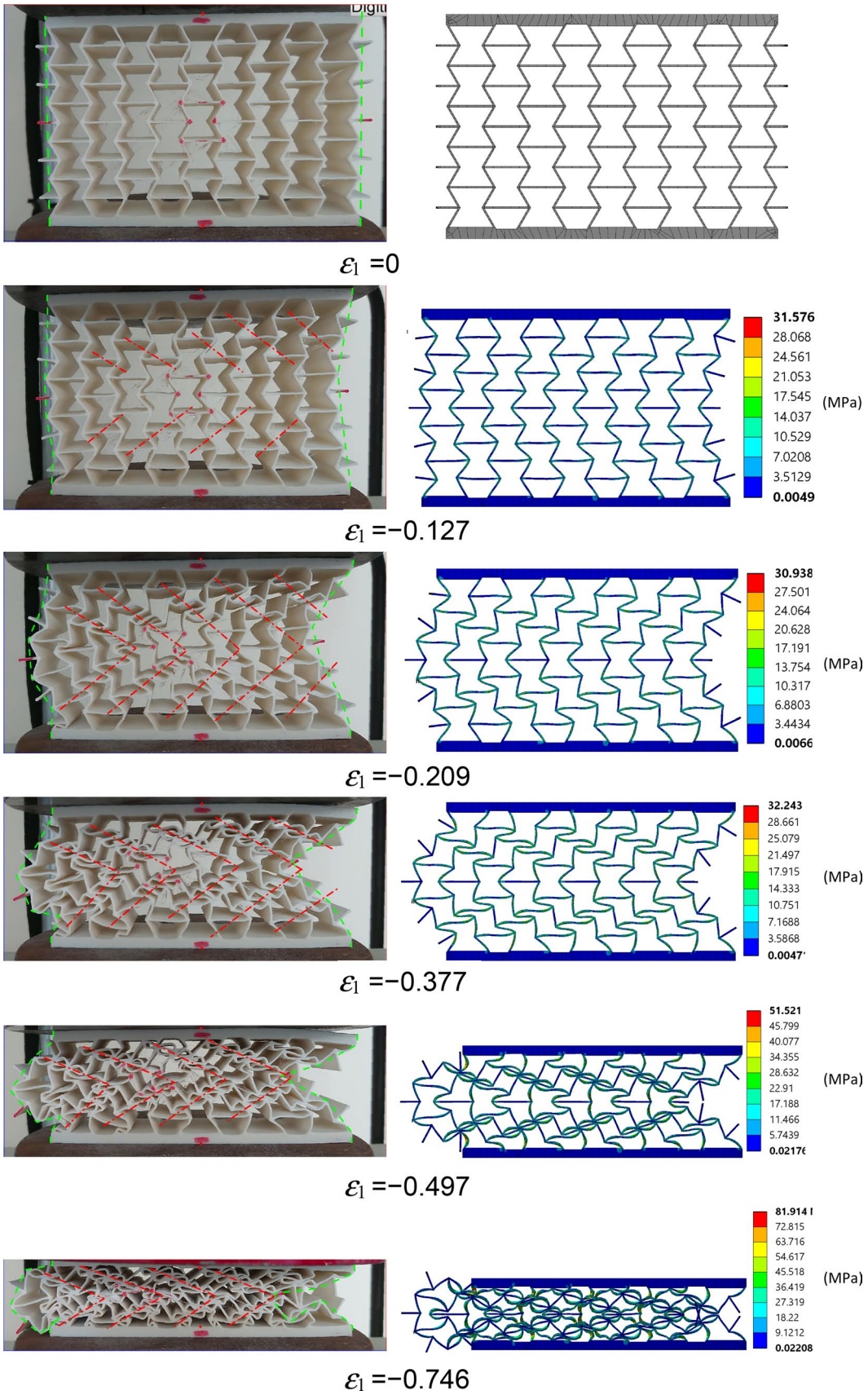

Fig. 7 The deformation history of CRC tiled structure

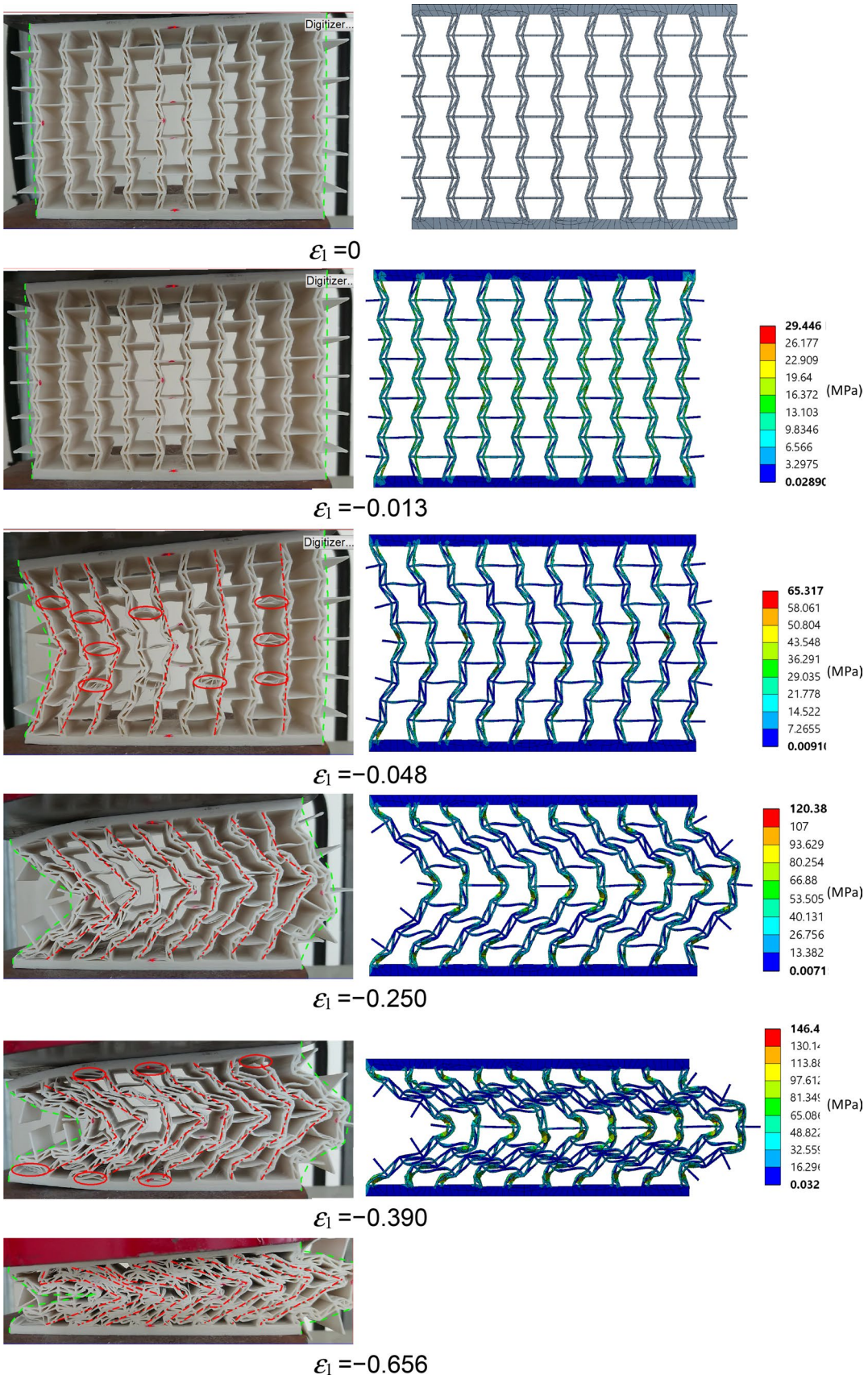

Fig. 8 The deformation history of Type-I cell tiled structure

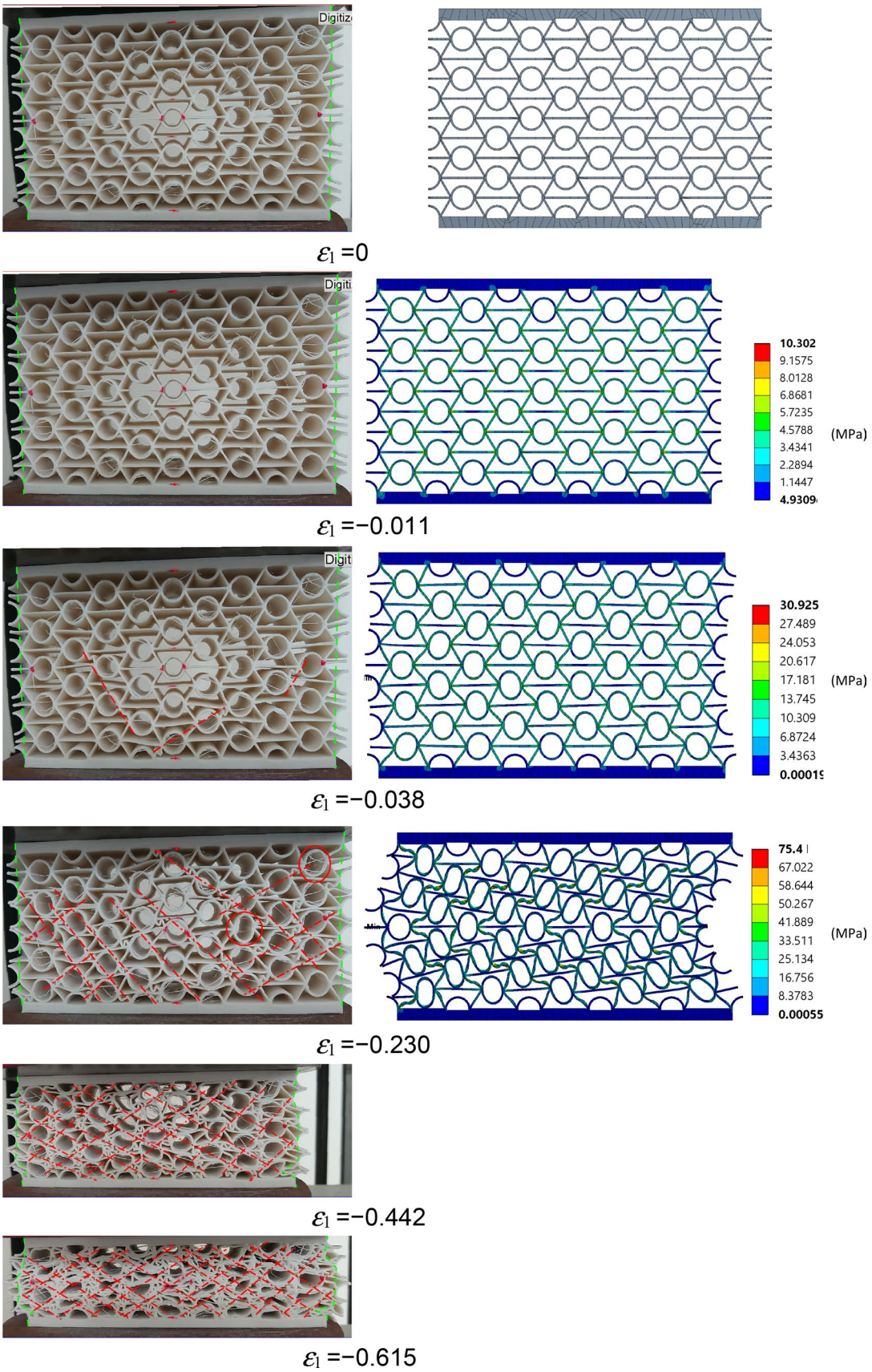

Fig. 9 The deformation history of Type-II cell tiled structure

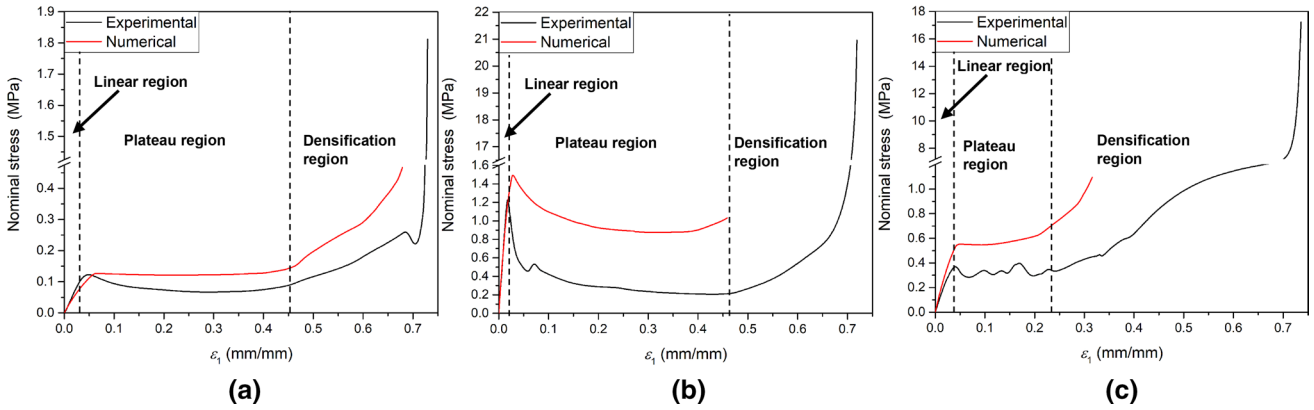

Fig. 10 Experimental and numerical nominal stress–strain curves of cells: **a** CRC tiled structure; **b** Type-I cell tiled structure; **c** Type-II cell tiled structure

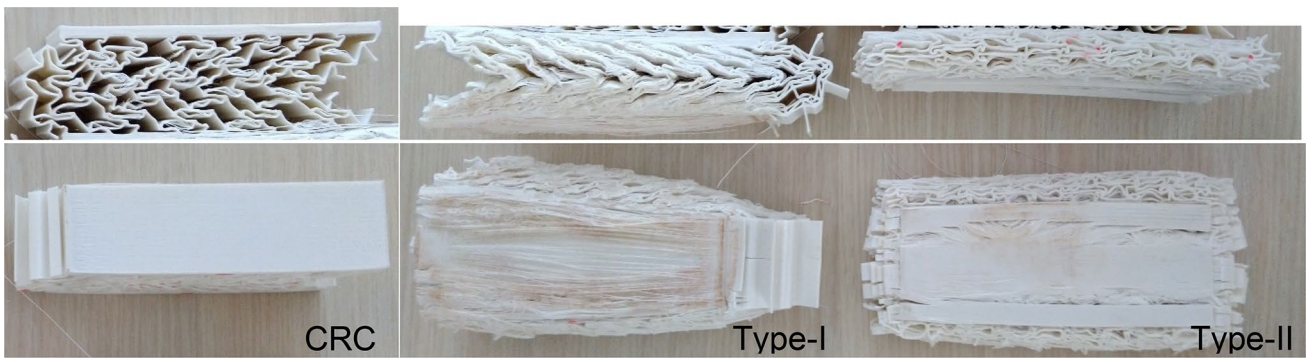

Fig. 11 Fully crushed specimens

From Fig. 7, the compression behaviour of the CRC tiled structure can be evaluated in detail: as seen from both in the numerical and the experimental results, with the buckling of the horizontal cell walls that are located at the up and the bottom of the centreline, the whole structure buckles in one way. The horizontal cell walls along the structural centreline do not buckle in the numerical models different from the experiments. The directions of the buckled cell walls align with a regular "V" pattern that is indicated with dashed red lines in Fig. 7. The angle between the arms of "V" continues to decrease until the end of the loading. This pattern was introduced and named as "V" mode by Dong et al. [85]. Dong et al. [85] stated that this behaviour is related to thin-walled cells. Meanwhile, the inclined cell walls exhibit bending behaviour more than buckling. This finding is coherent with the modelling inclined wall as bending beams in the theoretical models [13, 77, 78].

Almost the same structural behaviour can be observed for Type-I cell tiled structure with those of the CRC tiled one, from Fig. 8. The behaviour of Type-I structure is governed by strengthened cell walls that became structural column like elements. With the loading, columns buckle simultaneously in the same direction. Different from the CRC, the inclined walls of Type-I do not buckle in the cell size level owing to large rigidity. A complete column buckling was observed from bottom to top of the structure. The structure inflates and becomes denser on the side of buckling owing to the folding of rigid columns on themselves. The horizontal cell walls exhibit a double-curved buckling behaviour, and early ruptures of these walls appear that stem from large stiffness of inclined walls. This behaviour is like the shear wall-beam connection behaviour in structural engineering. These rigid walls can bestow a very large shear strength to the Type-I structure along 2 direction and axial strength along 1 direction. A closer look at the last two steps of the numerical result reveals the bending of the walls out of the plane which is unexpected and not seen in the experiments. Despite all attempts to a successful solution, the numerical solution did not converge after the strain level of -0.390. The numerical solution did not converge after a certain displacement level. Hence FE software terminated the solution. Although in FE analyses, all boundary conditions were

Table 4 Calculated elasticity moduli of re-entrant cells

	Elasticity modulus (E_1) (MPa)				Variation (%)		
	Experimental	Numerical	Theoretical with eqs. of Baran and Ozturk [77], Tatlier et al. [78]		$e = Abs\left(\frac{C\#2-C\#3}{C\#2}\right) \times 100$	$e = Abs\left(\frac{C\#2-C\#4}{C\#2}\right) \times 100$	$e = Abs\left(\frac{C\#2-C\#5}{C\#2}\right) \times 100$
			with axis-to-axis l and h	with clear l			
CRC	3.241	3.090	2.692	3.468	4.659	16.939	7.004
Type-I	74.944	84.326	50.100	84.208	12.519	33.150	12.361
Type-II	12.658	19.928	10.388	10.590	57.434	17.933	16.337

defined to simulate the experimental conditions, the nonparallel deformation of the face plates could not be simulated in the numerical analyses.

The most distinctive difference was obtained between numerical and experimental results for Type-II as seen in Fig. 9. In the experiments, at first, inclined walls crushed. After the first circular wall collapses that are indicated with red circles in Fig. 9, a serial crushing of cells was observed. Somehow the behaviour was an independent cell behaviour more than a whole structural behaviour. All inclined walls collapsed with the mode of double-curved buckling. Then the circular walls that stand up the structure collapsed simultaneously. At the last phase, the whole structure was crushed with a pattern that may be named multiple "X" mode. The arms of the "X" pattern are mostly parallel to inclined cell walls. As seen from Fig. 9, the horizontal cell walls buckled nowhere in the structure due to the perfectly symmetrical behaviour and two-way support of deformed circular walls. The crushing of Type-II cell was the most brittle one of all cells and suddenly appeared. As with Type-I numerical analysis, also Type-II numerical analyses were terminated by the FE software at a certain level of displacement that can be seen in Fig. 9. Again, like Type-I, the out-of-plane bending of walls is also observed at the last step of numerical results of Type-II. The reason for this behaviour is increased stiffness and structural constraints of the modified cells, because out-of-plane bending did not appear in the CRC analyses. From the evaluation of the numerical results of all cells, it is understood that the numerically determined structural behaviour and experiments are consistent at a certain level.

From Fig. 11, a critical conclusion can be obtained: after the unloading of the structures, only the induced displacement of CRC tiled structures withdrew. Unlike the other two types, owing to its small density it was not possible to load the CRC structure until the walls merge. This behaviour can be interpreted as the CRC exhibiting more elastic behaviour than both Type-I and Type-II because of having more void. Also, the top view of the crushed specimens is evidence of having a positive Poisson's ratio of the modified cells after crushing. The CRC structure does not bulge across 3 direction as seen in Fig. 11. The dense cellular structures will exhibit plastic behaviour. Moreover, the loading limits of dense cellular structures should be set up carefully to avoid brittle collapses. Having a large stiffness leads more plastic deformations. The cell types and their design parameters should be scrutinized for the needs of the application.

Figure 10 depicts the nominal stress–strain relationships obtained from the experimental and numerical results of the specimens. The strain may be calculated using Eq. (1) and the nominal stress is obtained by:

$$\sigma_{11} = F_{11}/A \tag{4}$$

where σ_{11} is nominal stress; F_{11} is the load values obtained from the test machine data acquisition system in the experiments and the reaction forces in the numerical solution; A is the cross-sectional area of the specimen calculated by the multiplication of the width and length of the structure. From Fig. 10, a similar tendency with an amount of deviation can be observed between the available parts of numerical solutions and experiments. With a close look at the linear parts of the curves, this tendency became a quite good match. Figure 10a depicts a typical ductile material stress–strain curve obtained from the results of the CRC tiled structure. After the linear region where the strain level is between zero and 0.03, a plateau region starts that ends at around 0.45 strain level. Then a well-known auxetic material densification region evidently appears at the strain level 0.45. The curve comes to an end at about 1.8 MPa stress and 0.7 strain level. The plateau stress may be determined from the curve as 0.7 MPa. Owing to no sudden wall crushes, the stress–strain curve does not fluctuate. The CRC specimen draws an ideal smooth ductile curve that will be employed for the benchmark of the modified cells. Figure 10a also shows that there is quite good coherence between numerical and experimental results in means of structural behaviour.

Although their stress–strain curves seen in Fig. 10b tend almost the same, the difference between numerical and experimental results of Type-I appears the most distinctive one of all cell types (see Fig. 10). While numerical results plot an ideal stress–strain curve, some early collapses of cell walls and inclined wall lines cause a major oscillation on the experimental curve at the strain level of about 0.05. Just after the sudden crushes, developing wall-to-wall contacts strengthen the structure and stress rises for a short while. A second yield point appears at the stress level of 0.55 MPa and strain level of 0.072 after the first stress–strain yield point of 1.28 MPa, 0.018. After a brittle crush, the stress–strain curve plots a smooth plateau curve thanks to harmonious structural behaviour until the point of 0.20 MPa and 0.46 stress–strain. With infant wall-to-wall contacts smooth densification can be tracked from the curve. As soon as the curve passes the stress–strain point at the value of 0.84 MPa and 0.68, fully developed wall-to-wall contacts bestow quick and large densification until the full crush point that located at the point of 20.96 MPa and 0.72. The cell wall and the strong inclined wall line collapses that appear at the strain level of 0.048 can be seen in Fig. 8 with red ellipses and the red dashed line on the left side, respectively. The cell wall crushes may stem from the high rigidity of the inclined walls. The laminated structure of horizontal walls is broken down by rigid inclined walls with the increasing load, and the behaviour quickly became nonlinear. The plateau stress of the Type-I tiled structure can be determined as 0.3 MPa from Fig. 10b. The numerical stress–strain curve of Type-I can be interpreted as follows: the smooth stress–strain curves can be obtained from the physical models with a nonlaminated or

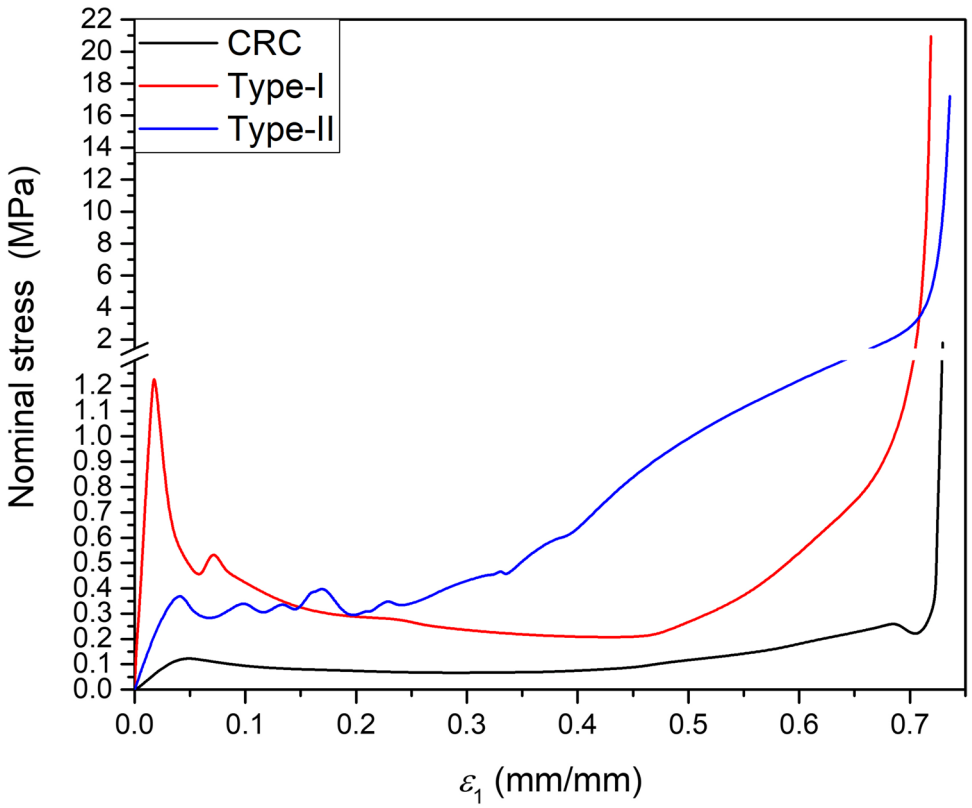

Fig. 12 Comparison of the experimental nominal stress–strain curves of structures

nonfibered monolithic fabrication of the walls. In any case, considering the material and structural uncertainties, the harmony of the numerical and the experimental results with an amount of offset is impressive and validates the numerical model.

The stress–strain curve of the Type-II tiled structure can be tracked from Fig. 10c as a ductile structural behaviour. Although they do not seem too similar in Fig. 9, the numerical and the experimental behaviour draws compatible stress–strain curves with an amount of offset. After the linear region ends at the point of 0.41 MPa and 0.042 stress–strain, a plateau region starts with fluctuations caused by the brittle collapses of inclined walls. The plateau region finalizes with the end of the fluctuations at the point of 0.32 MPa stress and 0.24 strain. This point is also where the end of the ductile crushes of the circular walls. Meanwhile, wall-to-wall contacts have already developed. The densification region appears with a low slope just after the end of the plateau region and quickly rises thanks to fully developed contacts. The densification is observed from the point of 0.32 MPa and 0.24 stress–strain to the endpoint of 17.23 MPa and 0.74 stress–strain. The plateau stress can be determined from the stress–strain curve as 0.3 MPa. The shortest plateau region belongs to Type-II among all types.

Evaluation of Figs. 8, 9, 11b, c together reveals an important finding: the nonconvergence and then the termination of the numerical analyses start with the complex contacts. The divergences in the analyses begin with the multiple contacts of the distant walls in Type-I analyses and the circular wall inner surface contacts in Type-II analyses. In the analyses, because the automatic surface-to-surface contacts option could not build the contacts, all contacts were defined one by one. The mentioned contacts were both nonpredictable and complex. Due to the predictable and noncomplex contacts, FE analyses of the CRC could be completed successfully. In addition, computer time consumptions of analyses were very high (approximately 1–2 days with Intel I7 7th gen quad-core CPU) and analyses required high-capacity CPUs.

A comparison between experimental, numerical, and theoretical results is presented in Table 4. The infrequent large error rates appear in Table 4 between experimental, numerical, and theoretical results. These errors may be stem from the structural uncertainties of 3D printed PLA wall material, e.g. the difficulty of modelling fibrous and layered printing, the poor-quality adhesion of layers, the printing errors. The experimental results give that while the density increments are 2.8 for Type-I and 1.78 for Type-II with respect to CRC, the elasticity moduli are 23.12 and 3.90 times larger than those of CRC, respectively. The close stiffness increment rates can also be determined utilizing the numerical and theoretical results. Please refer the appendices for the equations of analytical model.

The comparison of experimental results of specimens in Fig. 12 depicts improvement in the energy absorption ability of the cells. The energy absorption capacities were calculated from the area under the force–deflection curves which are the same tend as stress–strain curves that are no need to present here. The calculated areas under the experimental curves are 43.872 J, 173.183 J, and 350.068 J for CRC, Type-I, and Type-II, respectively. According to these results, the energy absorption capacities of Type-I and Type-II are 3.95 and 7.98 times larger than the CRC for a density increment of 2.8 and 1.78 times, respectively.

It should be remembered that although the rigidities and energy absorption capacities are increased in modified cells, the higher plasticity comes as a side product. This may be an important drawback for applications that are not desired plasticity. In this case, the loading limits and cell properties should be tuned for the requirement of the project. The supporting walls of the investigated cells Type-I and Type-II may be fabricated less stiff than the main walls to avoid brittle crushes using thickness and different materials options.

4 Conclusion

In this study, the experimental and numerical crushing results of two modified re-entrant cells that based on classical re-entrant cell are presented. These modified cells were introduced and studied by the authors in their previous papers. In this paper, comparisons of the experimental, numerical, and theoretical results indicate a quite well match in means of negative Poisson's ratios and elastic moduli, in the linear region. Besides that, almost the same structural behaviour was achieved in the nonlinear numerical analyses as experiments. Although in some numerical analyses, the structures could not be loaded until the last limits, with an amount of offset, similar stress–strain curves and load–deflection histories were obtained between numerical analyses and experiments. The mentioned findings depict that the experiments validate the numerical and theoretical models.

Results of this work reveal some design hints about re-entrant cells. A simple support to the inclined walls of the cell bestows to cell higher stiffness and energy absorption capacity while preserving its auxetic behaviour. However, large stiffness brings brittle crushes. To maintain high elastic behaviour, cell voids should be preserved as much as possible. Whether they are stiffened or not, re-entrant cells easily cross from linear to nonlinear regions even if they are subjected to a very low displacement. Particularly stiffened and became dense cell behaviours govern by wall-to-wall multiple contacts after the inclined wall crushes. After the full contacts, the structure can be loaded until the full

crush and cell walls fuse into each other. On the contrary to the dense cells, conventional re-entrant cell walls do not fuse into each other and when the structure is unloaded, an amount of induced displacement withdraw. Meanwhile, at the full crush, the conventional cell tiled structure does not swell along the axis that is perpendicular to the loading plane, unlike stiffened cell tiled one.

While designing cellular structures with desirable mechanical properties, the advantages and drawbacks mentioned above should be considered.

Appendix

Note that while calculating the classical re-entrant cell's mechanical properties it should be employed with very low stiffness and low cross-sectional parameters for the strengthening walls of the modified cells in the following equations.

(a) Type-I cell equations:

All equations of the Type-I cell may be derived from the deformation of the inclined walls. Employing inclined inner and outer walls on the quarter cell, the equations may be derived employed in this paper (for further information please refer to Baran and Ozturk [77]). Poisson's ratio and elasticity modulus of the Type-I cell may be expressed as:

$$\nu_{12} = -\frac{\left(2\frac{A_1E_{s1}\cos(\theta_1)^2\sin(\theta_1)}{l_2\cos(\theta_2)} + \frac{A_2E_{s2}\cos(\theta_2)\sin(\theta_2)}{l_2} + \frac{12E_{s2}I_2\sin(\theta_2)\cos(\theta_2)}{{l_2}^3(\alpha_2+1)} + \frac{24E_{s1}I_1\sin(\theta_1)\cos(\theta_1)^4}{{l_2}^3\cos(\theta_2)^3\left(\alpha_1\frac{\cos(\theta_1)^2}{\cos(\theta_2)^2}+1\right)}\right)\left(l_2\cos(\theta_2)+\frac{t_2}{2}\right)}{\left(2\frac{A_1E_{s1}\sin(\theta_1)^2\cos(\theta_1)}{l_2\cos(\theta_2)} + \frac{A_2E_{s2}\sin(\theta_2)^2}{l_2} + \frac{12E_{s2}I_2\cos(\theta_2)^2}{{l_2}^3(\alpha_2+1)} + \frac{24E_{s1}I_1\cos(\theta_1)^5}{{l_2}^3\cos(\theta_2)^3\left(\alpha_1\frac{\cos(\theta_1)^2}{\cos(\theta_2)^2}+1\right)}\right)(h+l_2\sin(\theta_2))} \tag{5}$$

$$E_1 = \frac{({K_1}^2 - K_2K_3)(l_2\cos(\theta_2)+\frac{t_2}{2})}{(2\frac{A_1E_{s1}\sin(\theta_1)^2\cos(\theta_1)}{l_2\cos(\theta_2)} + \frac{A_2E_{s2}\sin(\theta_2)^2}{l_2} + \frac{12E_{s2}I_2\cos(\theta_2)^2}{{l_2}^3(\alpha_2+1)} + \frac{24E_{s1}I_1\cos(\theta_1)^5}{{l_2}^3\cos(\theta_2)^3\left(\alpha_1\frac{\cos(\theta_1)^2}{\cos(\theta_2)^2}+1\right)})((h+l_2\sin(\theta_2))b_2)} \tag{6}$$

Appearing terms in equations may be given as:

$$K_1 = 2\frac{A_1E_{s1}\cos(\theta_1)^2\sin(\theta_1)}{l_2\cos(\theta_2)} + \frac{A_2E_{s2}\cos(\theta_2)\sin(\theta_2)}{l_2} + \frac{12E_{s2}I_2\sin(\theta_2)\cos(\theta_2)}{l_2^3(\alpha_2+1)} + \frac{24E_{s1}I_1\sin(\theta_1)\cos(\theta_1)^4}{l_2^3\cos(\theta_2)^3\left(\alpha_1\frac{\cos(\theta_1)^2}{\cos(\theta_2)^2}+1\right)} \tag{7a}$$

$$K_2 = 2\frac{A_1E_{s1}\cos(\theta_1)^3}{l_2\cos(\theta_2)} + \frac{A_2E_{s2}\cos(\theta_2)^2}{l_2} + \frac{12E_{s2}I_2\sin(\theta_2)^2}{l_2^3(\alpha_2+1)} + \frac{24E_{s1}I_1\sin(\theta_1)^2\cos(\theta_1)^3}{l_2^3\cos(\theta_2)^3\left(\alpha_1\frac{\cos(\theta_1)^2}{\cos(\theta_2)^2}+1\right)} \tag{7b}$$

$$K_3 = 2\frac{A_1E_{s1}\sin(\theta_1)^2\cos(\theta_1)}{l_2\cos(\theta_2)} + \frac{A_2E_{s2}\sin(\theta_2)^2}{l_2} + \frac{12E_{s2}I_2\cos(\theta_2)^2}{l_2^3(\alpha_2+1)} + \frac{24E_{s1}I_1\cos(\theta_1)^5}{l_2^3\cos(\theta_2)^3\left(\alpha_1\frac{\cos(\theta_1)^2}{\cos(\theta_2)^2}+1\right)} \tag{7c}$$

$$\alpha_1 = \frac{12E_{s1}I_1k_1}{{l_1}^2G_{s1}A_1} \tag{8a}$$

$$\alpha_2 = \frac{12E_{s2}I_2k_2}{{l_2}^2G_{s2}A_2} \tag{8b}$$

$$G_{s1} = \frac{E_{s1}}{2(1+\nu_{s1})} \tag{8c}$$

$$G_{s2} = \frac{E_{s2}}{2(1+\nu_{s2})} \tag{8d}$$

where ν_{12} is Poisson's ratio, E_1 is the elasticity modulus of the re-entrant cell, A_1 and A_2 are the cross-sectional areas of the inclined outer walls and inner wall, respectively, E_{s1} and E_{s2} are the elasticity moduli of the inclined outer walls' and inner wall's materials, respectively, θ_1 and θ_2 are the angles of the inclined outer walls and inner wall, respectively, I_1 and I_2 are the second moment of inertias of the inclined outer walls and inner wall, respectively, l_2 is the length of the inclined inner

wall, t_2 is the thickness of the inclined inner wall, h is the height of the re-entrant cell (length of the horizontal wall), b_2 is the width of the inclined wall, K_1, K_2, and K_3 are the stiffness terms that governs cell deformation, α_1 and α_2 are the shear deflection coefficients of the inclined outer walls and inner wall, respectively, k_1 and k_2 are the cross-section shear coefficients of the inclined outer walls and inner wall, respectively, l_1 is the length of the inclined outer walls, G_{s1} and G_{s2} are the shear moduli of the inclined outer walls' and inner wall's materials, respectively, ν_{s1} and ν_{s2} are Poisson's ratios of the inclined outer walls' and inner wall's materials, respectively.

(b) Type-II cell equations:

All equations of the Type-II cell may be derived from the deformation of the inclined and circular walls. Employing inclined and circular walls of the quarter cell, the equations may be derived employed in this paper (for further information please refer to Tatlıer et al. [78]). Poisson's ratio and elasticity modulus of the Type-II cell may be expressed as:

$$\nu_{12} = -\frac{\delta_{21}(Lcos(\theta) + \frac{t_2}{2})}{\delta_{11}(h + Lsin(\theta))} \tag{9}$$

$$E_1 = \frac{L\cos(\theta) + \frac{t_2}{2}}{\delta_{11}((h + L\sin(\theta)))b_2} \tag{10}$$

Appearing terms in equations may be given as:

$$\delta_{11} = \frac{K_{11}K_{23}\left(K_{33}{K_{12}}^2 + K_{11}{K_{23}}^2 - K_{11}K_{22}K_{33}\right) - K_{11}{K_{12}}^2K_{23}K_{33}}{{K_{11}}^2K_{23}\left(K_{33}{K_{12}}^2 + K_{11}{K_{23}}^2 - K_{11}K_{22}K_{33}\right)} \tag{11a}$$

$$\delta_{21} = \frac{K_{12}K_{33}}{\left(K_{33}{K_{12}}^2 + K_{11}{K_{23}}^2 - K_{11}K_{22}K_{33}\right)} \tag{11b}$$

$$K_{11} = \frac{A_2E_{s2}cos(\theta)^2}{L} + \frac{12E_{s2}I_2sin(\theta)^2}{L^3(1+\alpha)} \tag{12a}$$

$$K_{12} = \frac{12E_{s2}I_2cos(\theta)sin(\theta)}{L^3(1+\alpha)} - \frac{A_2E_{s2}cos(\theta)sin(\theta)}{L} \tag{12b}$$

$$K_{22} = \frac{12E_{s2}I_2\cos(\theta)^2}{L^3\left(1+\alpha_2\right)} + \frac{A_2E_{s2}\sin(\theta)^2}{L} + \frac{4\pi^2A_1E_{s1}G_{s1}^2I_1^2 - 32A_1^2E_{s1}G_{s1}^2I_1R^2 + 4\pi^2A_1E_{s1}^2G_{s1}I_1^2k' + 4\pi^2A_1^2E_{s1}G_{s1}^2I_1R^2}{D} \tag{12c}$$

$$K_{23} = \frac{32{A_1}^2E_{s1}{G_{s1}}^2{I_1}R^2 - 8\pi A_1E_{s1}{G_{s1}}^2{I_1}^2 - 8\pi{A_1}^2E_{s1}{G_{s1}}^2{I_1}R^2 + 8\pi A_1{E_{s1}}^2G_{s1}{I_1}^2k_1}{D} \tag{12d}$$

$$K_{33} = \frac{4\pi^2A_1E_{s1}{G_{s1}}^2{I_1}^2 - 32{A_1}^2E_{s1}{G_{s1}}^2{I_1}R^2 + 4\pi^2A_1{E_{s1}}^2G_{s1}{I_1}^2k_1 + 4\pi^2{A_1}^2E_{s1}{G_{s1}}^2{I_1}R^2}{D} \tag{12e}$$

G_{si}, α_i, R, and D that appear in equations above may be expressed as (where i is 1 for the circular wall and 2 for the inclined wall, respectively):

$$G_{si} = \frac{E_{si}}{2(1+\nu_{si})} \tag{13a}$$

$$\alpha_i = \frac{12E_{si}I_ik_i}{{L_i}^2G_{si}A_i} \tag{13b}$$

$$R = \frac{h}{2} + Lsin(\theta) \tag{13c}$$

$$\begin{aligned} D = {} & 32A_1^2G_{s1}^2R^5 + 32A_1G_{s1}^2I_1R^3 - 20\pi A_1^2G_{s1}^2R^5 \\ & + \pi^3A_1^2G_{s1}^2R^5 - 4\pi G_{s1}^2I_1^2R + \pi^3E_{s1}^2I_1^2Rk_1^2 \\ & - 24\pi A_1G_{s1}^2I_1R^3 + 2\pi^3A_1G_{s1}^2I_1R^3 - 4\pi E_{s1}^2I_1^2Rk_1^2 \\ & + 8\pi E_{s1}I_1^2G_{s1}Rk_1 - 32A_1E_{s1}G_{s1}I_1R^3k_1 + 2\pi^3E_{s1}G_{s1}I_1^2Rk_1 \\ & + 2\pi^3A_1E_{s1}G_{s1}I_1R^3k_1 - 8\pi A_1E_{s1}G_{s1}I_1R^3k_1 \end{aligned} \tag{13d}$$

where ν_{12} is Poisson's ratio, E_1 is the elasticity modulus of the re-entrant cell, δ_{11} and δ_{21} are the axial and the transverse displacement of cell, L is the length of inclined wall, t_2 is the thickness of the inclined wall, θ is the angle of the inclined wall, h is the height of the re-entrant cell (length of the horizontal wall), b_2 is the width of the inclined wall,

K_{ij} terms are the stiffness terms that govern cell deformation (where i and j indicate the cell's degrees of freedoms: 1 and 3 are along with 1 axis and 2 is along with 2 axis), A_1 and A_2 are the cross-sectional areas of the circular and inclined walls, respectively, E_{s1} and E_{s2} are the elasticity moduli of the circular and inclined walls' materials, respectively, I_1 and I_2 are the second moment of inertias of the circular and inclined walls, respectively, h is the height of the re-entrant cell (length of the horizontal wall), b_2 is the width of the inclined wall, α_i terms are the shear deflection coefficients of the circular and inclined walls, k_i terms are the cross-sectional shear coefficients of the circular and inclined walls, G_{si} terms are the shear moduli of the circular and inclined walls, ν_{si} terms are Poisson's ratios of the circular and inclined walls' materials, R is the radius of the circular wall, and D is the determinant of the structural matrix of the cell.

Supplementary Information The online version contains supplementary material available at https://doi.org/10.1007/s40430-022-03889-x.

Acknowledgements This work was partially supported by The Scientific and Technological Research Council of Turkey (TUBITAK, Project No: 119M180)

Author contributions MÖ helped in formal analysis, resources, visualization, writing—original draft, investigation, data curation, experimental work. TB contributed to conceptualization, methodology, validation, resources, writing—original draft, writing—review and editing, project administration, experimental work. MST was involved in conceptualization, validation, resources, supervision, writing—review and editing.

Data availability All the data used in this manuscript can be obtained on request from the corresponding author.

Code availability There is no special code generated for this research.

Declarations

Conflict of interest The authors declare that they have no conflict of interest.

References

1. Saxena KK, Das R, Calius EP (2016) Three decades of auxetics research—materials with negative Poisson's ratio: a review. Adv Eng Mater 18:1847–1870. https://doi.org/10.1002/adem.201600053
2. Gibson LJ, Ashby MF (1997) Cellular solids structure and properties. Cambridge Solid State Science Series, Cambridge
3. Fung Y-C (1965) Foundations of solid mechanics. Prentice- Hall, New Jersey
4. Greaves GN, Greer AL, Lakes RS, Rouxel T (2011) Poisson's ratio and modern materials. Nature Materials, UK
5. Ting TCT, Chen T (2005) Poisson's ratio for anisotropic elastic materials can have no bounds. Quarterly J Mech Appl Math 58:73–82. https://doi.org/10.1093/qjmamj/hbh021
6. Williams JL, Lewis JL (1982) Properties and an anisotropic model of cancellous bone from the proximal Tibial epiphysis. J Biomech Eng 104:50–56. https://doi.org/10.1115/1.3138303
7. Lees C, Vincent JFV, Hillerton JE (1991) Poisson's ratio in skin. Bio-Med Mater Eng 1:19–23. https://doi.org/10.3233/BME-1991-1104
8. Frolich LM, LaBarbera M, Stevens WP (1994) Poisson's ratio of a crossed fibre sheath: the skin of aquatic salamanders. J Zool 232:231–252. https://doi.org/10.1111/j.1469-7998.1994.tb01571.x
9. Milstein F, Huang K (1979) Existence of a negative Poisson ratio in fcc crystals. Phys Rev B 19:2030–2033. https://doi.org/10.1103/PhysRevB.19.2030
10. Evans KE (1991) The design of doubly curved sandwich panels with honeycomb cores. Compos Struct. https://doi.org/10.1016/0263-8223(91)90064-6
11. Lakes RS (1979) (1987) Foam structures with a negative Poisson ' s ratio. Science 235:1038–1040. https://doi.org/10.1126/science.235.4792.1038
12. Gibson LJ, Ashby MF, Schajer GS, Robertson CI (1982) The mechanics of two-dimensional cellular materials. Proc R Soc Lond A382:25–42
13. Masters IG, Evans KE (1996) Models for the elastic deformation of honeycombs. Compos Struct 35:403–422. https://doi.org/10.1016/S0263-8223(96)00054-2
14. Larsen UD, Sigmund O, Bouwstra S (1996) Design and fabrication of compliant micromechanisms and structures with negative Poisson's ratio. In: Proceedings of the IEEE Micro Electro Mechanical Systems (MEMS)
15. Larsen UD, Signund O, Bouwsta S (1997) Design and fabrication of compliant micromechanisms and structures with negative Poisson's ratio. J Microelectromech Syst 6:99–106. https://doi.org/10.1109/84.585787
16. Grima JN, Gatt R, Alderson A, Evans KE (2005) On the potential of connected stars as auxetic systems. Mol Simul. https://doi.org/10.1080/08927020500401139
17. Smith CW, Grima JN, Evans KE (2000) Novel mechanism for generating auxetic behaviour in reticulated foams: missing rib foam model. Acta Mater 48:4349–4356. https://doi.org/10.1016/S1359-6454(00)00269-X
18. Lim T-C (2015) Auxetic materials and structures. Springer, Singapore
19. Alderson KL, Evans KE (2000) Auxetic materials: the positive side of being negative. Eng Sci Educ J 9:148–154. https://doi.org/10.1049/esej:20000402
20. Alderson A, Alderson KL (2007) Auxetic materials. Proc Inst Mech Eng, Part G: J Aero Eng 221:565–575. https://doi.org/10.1243/09544100JAERO185
21. Evans KE, Alderson A (2000) Auxetic materials: functional materials and structures from lateral thinking. Adv Mater 12:617–628. https://doi.org/10.1002/(SICI)1521-4095(200005)12:9%3c617::AID-ADMA617%3e3.0.CO;2-3
22. Lakes RS, Elms K (1993) Indentability of Conventional and Negative Poisson's ratio foams. J Compos Mater. https://doi.org/10.1177/002199839302701203
23. Dirrenberger J, Forest S, Jeulin D (2013) Effective elastic properties of auxetic microstructures: anisotropy and structural applications. Int J Mech Mater Des 9:21–33. https://doi.org/10.1007/s10999-012-9192-8
24. Evans KE (1991) Auxetic polymers: a new range of materials. Endeavour 15:170–174. https://doi.org/10.1016/0160-9327(91)90123-S
25. Ju J, Summers JD, Ziegert J, Fadel G (2009) Design of honeycomb meta-materials for high shear flexure. In: 35th Design automation conference, Parts A and B. ASMEDC

26. Lira C, Innocenti P, Scarpa F (2009) Transverse elastic shear of auxetic multi re-entrant honeycombs. Compos Struct 90:314–322. https://doi.org/10.1016/j.compstruct.2009.03.009
27. Schultz J, Griese D, Ju J et al (2012) Design of honeycomb mesostructures for crushing energy absorption. J Mech Des 134:071004. https://doi.org/10.1115/1.4006739
28. Shankar P, Ju J, Summers JD, Ziegert JC (2010) Design of sinusoidal auxetic structures for high shear flexure. In: 30th Computers and information in engineering conference, Parts A and B
29. Shankar P, Fazelpour M, Summers JD (2013) An energy-based design approach for a meso-structure with high shear flexure. In: 39th Design automation conference. American Society of Mechanical Engineers
30. Spadoni A (2011) An isotropic auxetic structural network with limited shear stiffness. In: Mechanics of solids, structures and fluids; vibration, acoustics and wave propagation. ASMEDC
31. Choi JB, Lakes RS (1996) Fracture toughness of re-entrant foam materials with a negative Poisson's ratio: experiment and analysis. Int J Fract 80:73–83. https://doi.org/10.1007/BF00036481
32. Scarpa F, Giacomin JA, Bezazi A, Bullough WA (2006) Dynamic behavior and damping capacity of auxetic foam pads. In: Smart structures and materials 2006: Damping and Isolation
33. Ruzzene M, Scarpa F, Soranna F (2003) Wave beaming effects in two-dimensional cellular structures. Smart Mater Struct 12:363–372. https://doi.org/10.1088/0964-1726/12/3/307
34. Phani AS, Woodhouse J, Fleck NA (2006) Wave propagation in two-dimensional periodic lattices. J Acoust Soc Am 119:1995–2005. https://doi.org/10.1121/1.2179748
35. Shiyin X, Xiuchang H, Hongxing H (2015) A study on the isolation performance of trichiral lattices with gradient geometry. J Vib Control 21:3465–3475. https://doi.org/10.1177/1077546314524261
36. Spadoni A, Ruzzene M, Gonella S, Scarpa F (2009) Phononic properties of hexagonal chiral lattices. Wave Motion. https://doi.org/10.1016/j.wavemoti.2009.04.002
37. Zhu R, Liu XN, Hu GK et al (2014) A chiral elastic metamaterial beam for broadband vibration suppression. J Sound Vib 333:2759–2773. https://doi.org/10.1016/j.jsv.2014.01.009
38. Bacigalupo A, Gambarotta L (2014) Homogenization of periodic hexa- and tetrachiral cellular solids. Compos Struct. https://doi.org/10.1016/j.compstruct.2014.05.033
39. Liebold-Ribeiro Y, Körner C (2014) Phononic band gaps in periodic cellular materials. Adv Eng Mater 16:328–334. https://doi.org/10.1002/adem.201300064
40. Bacigalupo A, De Bellis ML (2015) Auxetic anti-tetrachiral materials: equivalent elastic properties and frequency band-gaps. Compos Struct. https://doi.org/10.1016/j.compstruct.2015.05.039
41. Choi JB, Lakes RS (1995) Analysis of elastic modulus of conventional foams and of re-entrant foam materials with a negative Poisson's ratio. Int J Mech Sci. https://doi.org/10.1016/0020-7403(94)00047-N
42. Huang J, Zhang Q, Scarpa F et al (2017) In-plane elasticity of a novel auxetic honeycomb design. Compos B Eng 110:72–82. https://doi.org/10.1016/j.compositesb.2016.11.011
43. Korner C, Liebold-Ribeiro Y (2015) A systematic approach to identify cellular auxetic materials. Smart Mater Struct. https://doi.org/10.1088/0964-1726/24/2/025013
44. Lakes R (1991) Experimental micro mechanics methods for conventional and negative poisson's ratio cellular solids as cosserat continua. J Eng Mater Technol, Trans ASME. https://doi.org/10.1115/1.2903371
45. Spadoni A, Ruzzene M (2012) Elasto-static micropolar behavior of a chiral auxetic lattice. J Mech Phys Solids. https://doi.org/10.1016/j.jmps.2011.09.012
46. Auffray N, Dirrenberger J, Rosi G (2015) A complete description of bi-dimensional anisotropic strain-gradient elasticity. Int J Solids Struct. https://doi.org/10.1016/j.ijsolstr.2015.04.036
47. Dirrenberger J, Forest S, Jeulin D, Colin C (2011) Homogenization of periodic auxetic materials. Procedia Eng 10:1847–1852. https://doi.org/10.1016/j.proeng.2011.04.307
48. Doyoyo M, Wan HuJ (2006) Plastic failure analysis of an auxetic foam or inverted strut lattice under longitudinal and shear loads. J Mech Phys Solids 54:1479–1492. https://doi.org/10.1016/j.jmps.2005.12.007
49. Shokri Rad M, Prawoto Y, Ahmad Z (2014) Analytical solution and finite element approach to the 3D re-entrant structures of auxetic materials. Mech Mater 74:76–87. https://doi.org/10.1016/j.mechmat.2014.03.012
50. Shokri Rad M, Ahmad Z, Alias A (2015) Computational approach in formulating mechanical characteristics of 3D star honeycomb auxetic structure. Adv Mater Sci Eng 2015:650769. https://doi.org/10.1155/2015/650769
51. Imbalzano G, Tran P, Ngo TD, Lee PVS (2016) A numerical study of auxetic composite panels under blast loadings. Compos Struct. https://doi.org/10.1016/j.compstruct.2015.09.038
52. Imbalzano G, Linforth S, Ngo TD et al (2018) Blast resistance of auxetic and honeycomb sandwich panels: comparisons and parametric designs. Compos Struct. https://doi.org/10.1016/j.compstruct.2017.03.018
53. Qiao J, Chen CQ (2015) Analyses on the in-plane impact resistance of auxetic double arrowhead honeycombs. J Appl Mech, Trans ASME. https://doi.org/10.1115/1.4030007
54. Clausen A, Wang F, Jensen JS et al (2015) Topology optimized architectures with programmable Poisson's ratio over large deformations. Adv Mater. https://doi.org/10.1002/adma.201502485
55. Wang XT, Li XW, Ma L (2016) Interlocking assembled 3D auxetic cellular structures. Mater Des 99:467–476. https://doi.org/10.1016/j.matdes.2016.03.088
56. Zhang G, Khandelwal K (2019) Computational design of finite strain auxetic metamaterials via topology optimization and nonlinear homogenization. Comput Methods Appl Mech Eng. https://doi.org/10.1016/j.cma.2019.07.027
57. Schwerdtfeger J, Wein F, Leugering G et al (2011) Design of auxetic structures via mathematical optimization. Adv Mater. https://doi.org/10.1002/adma.201004090
58. Zied K, Osman M, Elmahdy T (2015) Enhancement of the in-plane stiffness of the hexagonal re-entrant auxetic honeycomb cores. Phys Status Solidi (B) Basic Res 252:2685–2692. https://doi.org/10.1002/pssb.201552164
59. Dong Z, Li Y, Zhao T et al (2020) Experimental and numerical research on foam filled re-entrant cellular structure with negative Poisson's ratio. Mater Des 160:106679. https://doi.org/10.1080/17452759.2019.1644184
60. Hanssen AG, Girard Y, Olovsson L et al (2006) A numerical model for bird strike of aluminium foam-based sandwich panels. Int J Impact Eng 32:1127–1144. https://doi.org/10.1016/j.ijimpeng.2004.09.004
61. Hou X, Deng Z, Zhang K (2016) Dynamic crushing strength analysis of auxetic honeycombs. Acta Mech Solida Sin 29:490–501. https://doi.org/10.1016/S0894-9166(16)30267-1
62. Novak N, Hokamoto K, Vesenjak M, Ren Z (2018) Mechanical behaviour of auxetic cellular structures built from inverted tetrapods at high strain rates. Int J Impact Eng 122:83–90. https://doi.org/10.1016/j.ijimpeng.2018.08.001
63. Dirrenberger J, Forest S, Jeulin D (2012) Elastoplasticity of auxetic materials. In: Computational materials science
64. Mizzi L, Grima JN, Gatt R, Attard D (2019) Analysis of the Deformation Behavior and Mechanical Properties of Slit-Perforated Auxetic Metamaterials. Phys Status Solidi (B) Basic Res 256:1–15. https://doi.org/10.1002/pssb.201800153

65. Mizzi L, Attard D, Gatt R et al (2020) Implementation of periodic boundary conditions for loading of mechanical metamaterials and other complex geometric microstructures using finite element analysis. Eng Comput. https://doi.org/10.1007/s00366-019-00910-1
66. Mizzi L, Salvati E, Spaggiari A et al (2020) Highly stretchable two-dimensional auxetic metamaterial sheets fabricated via direct-laser cutting. Int J Mech Sci. https://doi.org/10.1016/j.ijmecsci.2019.105242
67. Evans KE, Nkansah MA, Hutchinson IJ (1994) Auxetic foams: modelling negative Poisson's ratios. Acta Metall Mater 42:1289–1294. https://doi.org/10.1016/0956-7151(94)90145-7
68. Xia Z, Zhang Y, Ellyin F (2003) A unified periodical boundary conditions for representative volume elements of composites and applications. Int J Solids Struct 40:1907–1921. https://doi.org/10.1016/S0020-7683(03)00024-6
69. Huang J, Gong X, Zhang Q et al (2016) In-plane mechanics of a novel zero Poisson's ratio honeycomb core. Compos B Eng. https://doi.org/10.1016/j.compositesb.2015.11.032
70. Fu M, Chen Y, Zhang W, Zheng B (2016) Experimental and numerical analysis of a novel three-dimensional auxetic metamaterial. Phys Status Solidi (B) 253:1565–1575. https://doi.org/10.1002/pssb.201552769
71. Li D, Yin J, Dong L, Lakes RS (2018) Strong re-entrant cellular structures with negative Poisson's ratio. J Mater Sci 53:3493–3499. https://doi.org/10.1007/s10853-017-1809-8
72. Chen Y, Fu M-H (2017) A novel three-dimensional auxetic lattice meta-material with enhanced stiffness. Smart Mater Struct 26:105029. https://doi.org/10.1088/1361-665X/aa819e
73. Chen Y, Fu M-H (2018) Design and modeling of a combined embedded enhanced honeycomb with tunable mechanical properties. Appl Compos Mater 25:1041–1055. https://doi.org/10.1007/s10443-017-9650-4
74. Ingrole A, Hao A, Liang R (2017) Design and modeling of auxetic and hybrid honeycomb structures for in-plane property enhancement. Mater Des 117:72–83. https://doi.org/10.1016/j.matdes.2016.12.067
75. Bezazi A, Scarpa F, Remillat C (2005) A novel centresymmetric honeycomb composite structure. Compos Struct 71:356–364. https://doi.org/10.1016/j.compstruct.2005.09.035
76. Rayneau-Kirkhope D (2018) Stiff auxetics: Hierarchy as a route to stiff, strong lattice based auxetic meta-materials. Sci Rep 8:12437. https://doi.org/10.1038/s41598-018-30822-x
77. Baran T, Öztürk M (2020) In-plane elasticity of a strengthened re-entrant honeycomb cell. Eur J Mech, A/Solids. https://doi.org/10.1016/j.euromechsol.2020.104037
78. Tatlıer MS, Öztürk M, Baran T (2021) Linear and non-linear in-plane behaviour of a modified re-entrant core cell. Eng Struct 234:111984. https://doi.org/10.1016/j.engstruct.2021.111984
79. Ratner BD, Hoffman AS, Schoen FJ, Lemons JE (2013) Biomaterials science an introduction to materials in medicine, 3rd edn. Elsevier, Amsterdam
80. ASTM-D638–14 (2014) Standard Test Method for Tensile Properties of Plastics. ASTM Standards
81. Morel S, Lespine C, Coureau JL et al (2010) Bilinear softening parameters and equivalent LEFM R-curve in quasibrittle failure. Int J Solids Struct. https://doi.org/10.1016/j.ijsolstr.2009.11.022
82. Eutionnat-Diffo PA, Chen Y, Guan J et al (2019) Stress, strain and deformation of poly-lactic acid filament deposited onto polyethylene terephthalate woven fabric through 3D printing process. Sci Rep. https://doi.org/10.1038/s41598-019-50832-7
83. Ansys® (2018), Academic Research Mechanical, Release 18.1, Help System, ANSYS, Inc.
84. Meena K, Singamneni S (2021) Novel hybrid auxetic structures for improved in- plane mechanical properties via additive manufacturing. Mech Mater. https://doi.org/10.1016/j.mechmat.2021.103890
85. Dong Z, Li Y, Zhao T et al (2019) Experimental and numerical studies on the compressive mechanical properties of the metallic auxetic reentrant honeycomb. Mater Des. https://doi.org/10.1016/j.matdes.2019.108036
86. Alomarah A, Masood SH, Sbarski I et al (2020) Compressive properties of 3D printed auxetic structures: experimental and numerical studies. Virtual Phys Prototyp 15:1–21. https://doi.org/10.1080/17452759.2019.1644184
87. Novak N, Vesenjak M, Krstulović-Opara L, Ren Z (2018) Mechanical characterisation of auxetic cellular structures built from inverted tetrapods. Compos Struct 196:96–107. https://doi.org/10.1016/j.compstruct.2018.05.024
88. Qi C, Jiang F, Remennikov A et al (2020) Quasi-static crushing behavior of novel re-entrant circular auxetic honeycombs. Compos B Eng 197:108117. https://doi.org/10.1016/j.compositesb.2020.108117